



**UNIVERSITY
OF TRENTO - Italy**
DEPARTMENT OF INDUSTRIAL ENGINEERING

XXIX cycle

Doctoral School in Materials, Mechatronics
and Systems Engineering

High Temperature Sintering

**investigation of the dimensional precision and
mechanical properties of low alloyed steels**

Daniel Toledo dos Santos



June 2021

HIGH TEMPERATURE SINTERING

INVESTIGATION OF THE DIMENSIONAL BEHAVIOUR AND MECHANICAL PROPERTIES OF LOW ALLOYED STEELS

Daniel Toledo dos Santos

E-mail: d.toledodossantos@unitn.it

Approved by:

Prof. Alberto Molinari, Advisor
Department of Industrial Engineering
University of Trento, Italy.

Prof. Ilaria Cristofolini,
Department of Industrial Engineering
University of Trento, Italy.

Ph.D. Commission:

Prof. Christian Gierl-Mayer ,
Institute of Chemical Technologies and
Analytics
TU Wien, Austria.

Prof. Monica Campos Gómez,
Department of Materials Science and
Engineering.
University Carlos III of Madrid, Spain.

Prof. Cinzia Menapace,
Department of Industrial Engineering.
University of Trento, Italy.

University of Trento,
Department of Industrial Engineering

June 2021

**University of Trento - Department of
Industrial Engineering**

Doctoral Thesis

**Daniel Toledo dos Santos - 2021
Published in Trento (Italy) – by University of Trento**

ISBN: - - - - -

To my little ones, Sophia and Olivia.

Preface

This thesis was possible because of the partnership between industrial companies, EPMA (European Powder Metallurgy Association) and the University of Trento.

From the academic side, the research group headed by Professors Alberto Molinari and Ilaria Cristofolini has been working on projects related to powder metallurgy for a few decades and this experience is of extreme relevance to the industry and to materials science & engineering.

EPMA served not only as the main gear between the companies and the academic institution, but also providing an ecosystem for the powder metallurgy industry to evolve and elaborate world class research, such as the one that gave birth to this thesis.

The industrial partners of this project were:

Höganäs AB – Iron and metal powders supplier.

GKN Hoeganaes – High-volume ferrous powders for powder metallurgy and additive manufacturing supplier.

Pometon SpA – Supplier of ferrous and nonferrous metallic powders.

Ames – Sintered components manufacturer, one of the world leaders in the manufacturing of sintered parts, based in Spain, Hungary, USA, China.

GKN Sinter Metals – Producer of PM parts of the world.

Miba – Supplier of automotive industries, whose portfolio includes sintered components, industrial bearings, friction materials and powder electronic components.

Schunk – Supplier of products made of carbon, technical ceramics and sintered metals, from environmental simulation and air conditioning to ultrasonic welding and optical machines.

Onejoon GmbH – Furnace manufacturer and thermal solutions based in Germany.

Riedhammer – Kiln plant manufacturer.

Sacmi – Manufacturer of machines and complete plants for Ceramics, Packaging-Beverage, Food and Automation industries

The project was coordinated by Dr. Volker Arnhold, Powder Metallurgy Solutions, and Dr. Vladimir Kruzhanov (PM Consulting).

The author acknowledges the EPMA for organizing this project and the industrial partners for providing the resources for this project.

Abstract

The automobile industry has set the demand regarding Powder Metallurgy (PM) parts for decades, since this near-net shape technology is a cost-effective manufacturing process allying good mechanical properties with dimensional and geometrical precision. Aiming at the future of the electric automobiles high production and demand, many changes are on the way to guarantee the competitiveness of PM against other manufacturing process. The high costs of alloying elements such as Ni and Cu, the changes in health and safety regulations as well as light weighting of components are the topics of major importance in the field of PM and focus of main R&D around the globe. The use of high temperature sintering and different alloying elements are possible solutions to overcome properties obtained by using Ni as an alloying element sintered at conventional temperatures.

Materials with Cr, Mo and Si were investigated using high temperature sintering (1180°C and 1250°) in comparison to traditionally high Ni materials sintered at conventional temperature (1120°C). The dimensional stability, geometrical precision, density, and microstructure of ring-shaped specimens were studied by using a coordinate measuring machine (CMM) and the effect of HTS on the mechanical properties were estimated through the fraction of the load bearing section.

The effect of HTS on the dimensional precision and geometrical stability was later investigated in real parts manufactured by industrial partners through an EPMA Club Project. The 4%Ni material sintered at 1120°C was also compared to Ni-less/Ni-free materials sintered at 1250°C using tensile testing, impact testing, and hardness.

The use of HTS to improve the mechanical properties without impairing the dimensional and geometrical stability was confirmed in parts with both low and high complexity designs. This project sets the blueprint for future material developments using HTS as manufacturing process.

Table of contents

| | |
|---|-----------|
| Preface | 7 |
| Abstract | 10 |
| 1.Introduction | 11 |
| 2. State of the art | 14 |
| 2.1. Sintering | 14 |
| 2.2. Influence of high temperature sintering in the mechanical properties | 16 |
| 2.3. Influence of high temperature sintering in the dimensional change and precision..... | 20 |
| 2.4. High temperature sintering and the oxi-reduction of Cr and Mn alloys.... | 21 |
| 3. Experimental Procedure | 26 |
| 3.1 Materials, parts and processing | 26 |
| 3.2 Measurement of parts..... | 30 |
| 3.3 Density and microstructure | 33 |
| 3.4 Mechanical properties | 35 |
| 4. Results and Discussion | 37 |
| 4.1. High Temperature Sintering – Part A..... | 37 |
| 4.1.1. Densification..... | 37 |
| 4.1.2. Dimensional measurements | 39 |
| 4.1.3. Dimensional changes..... | 43 |
| 4.1.4 Geometrical characteristics..... | 45 |
| 4.1.5. Microstructure | 50 |
| 4.1.6. Estimation of the effect of the sintering temperature on mechanical properties | 66 |
| 4.2. High Temperature Sintering – Part B..... | 68 |
| 4.2.1. Density and porosity | 68 |
| 4.2.2. Dimensional measurements | 69 |
| 4.2.3. Dimensional changes..... | 75 |
| 4.2.3. Geometrical characteristics..... | 78 |
| 4.2.4. Pore characteristics | 82 |
| 4.2.6. Microstructural analysis | 86 |

| | |
|---------------------------------------|------------|
| 4.2.7. Hardness analysis..... | 93 |
| 4.2.8. Mechanical properties..... | 95 |
| 5. Conclusions..... | 99 |
| 6. Appendix A..... | 102 |
| 7. Appendix B..... | 105 |
| 8. Appendix C..... | 109 |
| 9. References..... | 111 |
| 10. Scientific production..... | 117 |
| 11. Acknowledgements..... | 118 |

1. Introduction

Powder Metallurgy (PM) is a process that consists in manufacturing nearly net-shaped components from raw materials made of metallic powder that is mixed, compacted in a rigid die and then go through a thermal process that will provide the final physical and mechanical properties, called sintering. [1]. The sintering process is responsible for the formation of the metallic bonding between the particles, the solubilization of alloying elements in the base powder and the transformation of a very disperse system, characterized by high free energy, into a more stable, with lower porosity and free energy system. In multiphase systems with components that are soluble among themselves (like Iron and Nickel powders), this process is associated to the elimination of nonequilibrium phases and the reduction of the chemical gradients [2].

Nickel is an alloying element traditionally used in the PM industry as an enhancer for toughness and strength of steels. The Ni alloyed powders are obtained by the diffusion bonding process, where nickel and coarse iron particles are bonded to mitigate the segregation of each element without compromising the compressibility of pure iron.

Two main concerns are connected to the future of Nickel in the PM industry. One is connected to its use in the manufacturing of batteries for electric automobiles. Each electric automobile carries sets of batteries that contain around 37kg of Nickel in its composition. The major investment banks and consulting firms around the globe present a growing consensus that electric automobile production may increase from 10 to 20 times in the next decade [3]. The high demand for electric vehicles might lead to an increase in nickel prices globally since the lack of investments from the Nickel industry made the production increase only 10% from 2014 to 2020 [4]. The second concern is regarding the nickel inhalable limits becoming stricter in the next years by the European health and safety regulators [5]. The increase in Nickel prices

and its impact in production costs might turn Nickel into an uncertainty for its future applications in the PM industry.

By removing or simply reducing the Nickel element from the traditionally used alloys, it is expected a reduction in the mechanical properties of Powder Metallurgy components. However, high temperature sintering (HTS) could be a possible solution to overcome the lack of mechanical properties due the reduction of Nickel in its composition. This process is characterized by the increase in the sintering temperature from the conventional 1120-1150°C to 1250°C, it is usually employed in the sintering of Chromium alloyed steels to activate the carbothermal reduction of the highly stable chromium oxide on the surface of powder particles [6]. Additionally, the increase in sintering temperature brings benefits such as, increased density, better pore morphology and hence the improvements in fraction of the load-bearing section. This results positively affect the mechanical properties [7,8]. For this reason, HTS is applicable to surpasses the issues of using no or low Nickel content in material composition.

Dimensional and geometrical precision are key factors when HTS is discussed for large scale applications in the press and sinter industry. The green parts present excellent dimensional precision, that is slightly worsened by sintering process [9]. Good dimensional and geometrical precision results were obtained in press and sinter parts sintered at high temperature (up to 1300°C) using a small batch vacuum furnace [10-11]. These results were confirmed using a continuous furnace with HTS [12].

In the context of Nickel element and its future in the PM industry, a consortium of several industrial partners, the EPMA and the University of Trento was established with the aim to study the influence of HTS on the dimensional and geometrical stability and the mechanical properties of low alloyed steels manufactured in industrial plants. A material with 4% Nickel was used as baseline to compare with Ni-less/Ni-free materials sintered at high temperature. Ring-shaped specimens were produced in the first part of the project to better understand the dimensional and geometrical behaviour. The influence of HTS on the mechanical properties was estimated using microstructural analysis allied to the determination of the fraction of

the load-bearing section. After this preliminary investigation, a second step of the project was designed aimed at:

1. verifying on real parts characterized by a complex geometry the dimensional and geometrical precision achievable when sintering at high temperature.
2. measuring mechanical properties of materials sintered at high temperature in comparison to those of the 4% Ni alloyed steel sintered at standard temperature, taken as reference.

Three real parts from the portfolio of products of the part manufacturers were chosen and produced with the Ni-less/Ni-free materials. In addition, tensile and impact specimens were manufactured. In the whole of the project, specimens and parts were produced by the industrial partners in the typical conditions of the industrial production.

The scope of the project was:

1. to verify if sintering at high temperature may impair the dimensional and geometrical precision of press-and-sintered parts.
2. the determine if and how much the sintering at high temperature may compensate for the reduction or elimination of Ni in the composition of the steel, thanks to the improvement of density and of pore morphology

2. State of the art

2.1. Sintering

As it is well known in the manufacturing industry, the Powder Metallurgy is capable of producing parts with almost no waste and with very high precision when compared to other production process [13]. The high competitiveness of using this manufacturing process, specifically the press and sinter (P&S) technology, is not only connected to the dimensional precision, but also to the lower impact to the environment allied to the good mechanical properties obtained in the final produced parts. The combination of these advantages is connected to some factors, such as [14]:

- Powder manufacturing process,
- Composition of the powder mix,
- Compaction process design and characteristics,
- Sintering process characteristics,
- Tooling and types of equipment used.

The metallic powder can be obtained mainly by mechanical processes like friction and milling; by physical processes such as gas or water atomization; or by chemical processes through thermochemical, precipitation or electrolytic methods.

In the production of steels, a wide variety of alloying elements can be used depending on the desired properties of the final components being produced, having of course, the iron element as main constituent in the powder mix.

As per the compaction process, many approaches have been developed in the recent years to better understand the influence of the compaction variables and the materials composition on the densification process [15-19], but further

investigation performed by Cristofolini et al [20] showed the trying to fit these equations into experimental densification curves still show some disagreement.

Following the production chain, the compacted powder particles (named green parts) that at this point already present modest mechanical properties due to a bonding process, must enter the sintering stage. It consists practically in inserting the green parts into a furnace that will heat them to a specific temperature (60% to 90% of the melting temperature) in a controlled environment, where the heating rate, the protective atmosphere and the cooling rate are controlled to provide the final mechanical properties to the component.

The sintering process is a thermal treatment that activates diffusion mechanisms responsible for the consolidation of the PM material either in solid or liquid state. The protective atmosphere is responsible for the prevention of oxidation and promotes the reduction of surface oxides responsible for inhibiting the sintering mechanisms. When the sintering temperature is increased from 1175°C up to 1425°C, the process is called high temperature sintering (HTS). Sintering activity is increased at high temperatures, leading to improved alloy diffusion and more developed sintering neck, both of which effectively increase the final density and the morphology of pores. These enhancements all contribute to improvement on the mechanical properties compared to conventional sintering method [21-22]

Some of the reasons for choosing HTS are its positive influence on the diffusion mechanisms and the improvements of density and pore morphology but as long as they do not impair the dimensional and geometrical stability of the final components. This is why studying the shrinkage and dimensional stability of the PM materials is so important. The relations between the use of HTS and the competitiveness of PM industry also depend on delivering components with mechanical properties fitting the requirements of the applications combined with dimensional and geometrical precision to avoid any post-sintering machining. In some cases, when Cr or Mn containing materials must be sintered, HTS is a requirement, due to the reductions of stable oxides that are achieved only in high temperatures.

The concepts and the studies covering each of these key factors through the years are covered in this chapter.

2.2. Influence of high temperature sintering in the mechanical properties

Lower mechanical properties are observed when porous sintered steels are compared to full dense steels with the same matrix and microhardness. This happens due to the porosity; it acts as a stress concentrator as well as it reduces the fraction of the load bearing section of the materials, affecting the mechanical properties. The influence of porosity on the mechanical properties depends on the pore morphology, its distribution, size, their interconnection, and quantity [23]. Figure 1 shows the influence of density and relative density and how it affects the tensile, fatigue and impact properties in comparison to the full dense material.

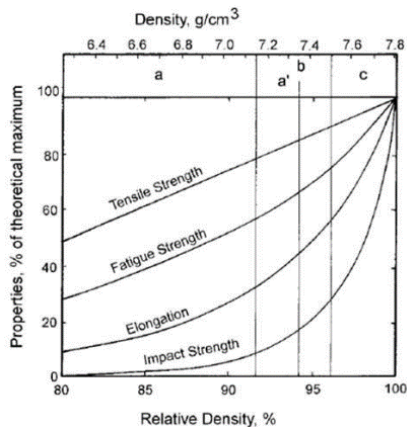


Figure 1 – Density and relative density in correspondence to the tensile properties of full dense ferrous alloys [24].

Puscas et al [25] have studied the influence of the high temperature sintering on the pore morphology of chromium steels. By performing image analysis on specimens sintered at 1120°C and 1250°C it was observed that increasing the sintering temperature improved the smoothness (f_{circle}) of the pores more than its

roundness (f_{shape}). Figure 2 shows the effect of the sintering temperature on f_{circle} and f_{shape} .

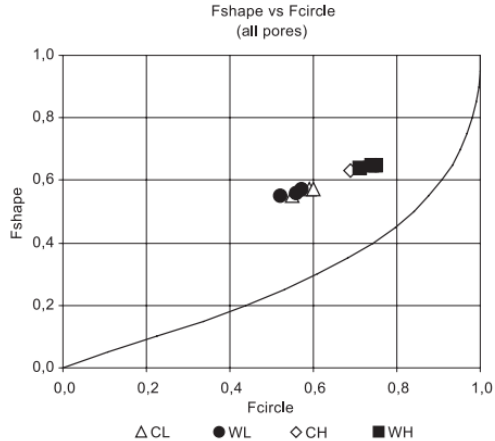


Figure 2 – Diagram of $f_{\text{shape}}-f_{\text{circle}}$ highlighting the effect of sintering temperature. CL and WL stand for cold and warm compacted specimens sintered at 1120°C, respectively. CH and WH stand for cold and warm compacted specimens sintered at 1250°C [25].

Beiss and Dalgic [26] have studied the influence of sintering temperature on density, pore morphology and the mechanical properties on a wide range of iron alloys, the results confirmed HTS enhances pore rounding. However HTS improves the fatigue resistance of PM materials, Beiss and Lindlohr [27] later highlighted that fatigue properties are predominantly controlled by the largest pores and not the average pore size or shape, by using the Murakami approach [28].

Toledo dos Santos et al [29] showed that increasing the sintering temperature of Mo-Ni-Cu steels improved the homogeneity of Ni-containing steels as well as the pore morphology, decreasing the porosity and hence improving the fraction of the load bearing section. Stoyanova and Molinari [30] used vacuum sintering and sinter-hardening at 1250°C to investigate the influence of HTS on Mo-Ni and Ni-free materials. The results showed that increasing the sintering temperature from 1120°C to 1250°C positively influences the tensile properties. Additionally, an increase of 25%

on the UTS was observed when the carbon content increased from 0,45% to 0,55% in the Ni-free materials. By combining high sintering temperature with an accelerated cooling rate, the performance of PM materials can be further improved. The quantity of martensite is increased by adding Ni, which results in a further enhancement of strength.

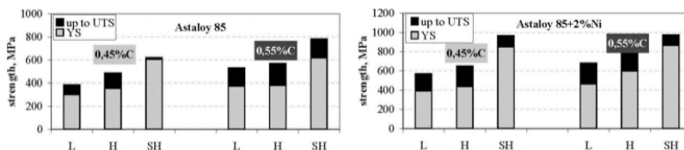


Figure 3 –Tensile strength: a) Ni-free materials; b) Ni-alloyed materials. L, H and SH stand for materials sintered at 1120°C, 1250°C and 1250°C sinter-hardened, respectively. [30]

Shen and Shivanath [31] performed tensile testing in specimens with Mo-Mn, sintered at 1140°C and 1300°C. Specimens with higher Mn presented higher increments on the tensile properties (20%) when compared to those sintered at conventional temperature (1140°C) while those with lower Mn content presented an increment of (7%) when the sintering temperature was raised.

The use of Mn as an alloying element is well diffused into the PM industry since the 90's [32] due to its low-cost and its influence on hardenability and on the mechanical properties that can be boosted using HTS. Manganese oxide equilibria is shown on Figure 4, which indicates the dew point necessary to reduce manganese oxide at different temperatures. Moreover, due to the strong tendency to oxidize, HTS with low dew points is always preferred to prevent oxidation of Mn element. Some studies still diverge about using HTS to obtain excellent homogenization of Mn in PM steels [33-34], but they converge when not orienting conventional sintering temperature to Mn-containing materials.

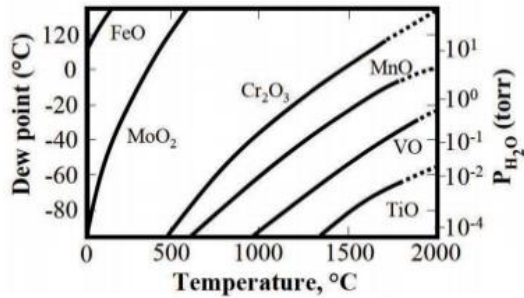


Figure 4 – Metal oxide equilibria in hydrogen [35].

Recently, different materials are being developed to overcome the volatility of some alloying element prices, such as Ni and Cu. Wimbert et al [36] researched materials using Si and V as alloying elements sintered in an Abbott belt furnace at 1260°C. The transverse rupture test (TRS) showed promising results even for Si-V materials when HTS is applied, opening a new path for materials using different alloying elements for applications related to the lightweight materials demand in the automobile industry as well [37-39].

Oro et al [40] explored the benefits of increasing the sintering temperature up to 1300°C using prealloyed and masteralloy approaches of materials containing Cr, Mn, and Si. The improvements on the mechanical properties were presented considering the evolution of the microstructure caused by the better diffusivity on increasing the sintering temperature as well as its positive effect on density, hardness, tensile properties, and impact energy.

The research performed by Sundaram [41] used one lab furnace and one industrial vacuum furnace under 4 different pressures (10, 1, 10⁻² and 10⁻⁴ mbar) to investigate the feasibility of Cr alloyed steels sintered at conventional and high temperature since modern developments in vacuum furnace technologies have led to an increased interest in vacuum sintering of PM parts. Density and carbon content were examined, and the results indicate an efficient oxide reduction and process robustness at intermediate vacuum levels, while HTS in high vacuum might enable Cr-sublimation. Vacuum sintering proved to be a requirement to process Cr-alloyed PM

steels. Stoyanova [42-43] also used vacuum furnace to sinter Cr-containing alloys and study the influence of microstructure and microhardness on impact properties of Cr-Mo specimens. The study indicated that microhardness might not be the best method to correlate with impact behaviour, although the positive aspects of HTS were highlighted as positively.

2.3. Influence of high temperature sintering in the dimensional change and precision

Different kinetic equations were developed in the past trying to explain the link between shrinkage behaviour and the diffusion mechanisms that are activated during the sintering process, but more recently, Baselli and Molinari [44] developed an equation involving the mass transport mechanism, material composition, sintering time, and temperature to explain the linear shrinkage of a sintered component.

Finally, Zago et al [45] researched an improved design method for PM parts and later Cristofolini et al [46] investigated the influence of complex geometries and how the density gradients can affect the shrinkage anisotropy.

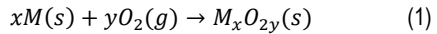
Cristofolini et al., also used GD&T point of view to study the influence of HTS on the dimensional changes and geometrical characteristics of PM parts. Starting the analysis from simple designs [47] and later analyzing more complex shapes [48], also considering the microstructure and density of each material. Specimens were sintered even at 1350°C without affecting dimensional and geometrical precision of steel parts. The studies also indicated that on increasing the sintering temperature, shrinkage also increases, and anisotropy of dimensional changes get progressively attenuated.

2.4. High temperature sintering and the oxi-reduction of Cr and Mn alloys.

One of the obstacles in the manufacturing of PM components is connected to the use of alloying elements that are sensitive to oxidation, a good example are Cr and Mn. The cost competitiveness of PM technology against other manufacturing processes is crucial when these alloying elements are used since Cr and Mn present lower cost when compared to traditional alloying elements such as Mo, Ni and Cu.

Sintering stage is the most important step in the manufacturing chain of this oxidation sensitive materials, since temperature and controlled atmosphere are the variables that regulate the stability of oxides present in the material.

Understanding the thermodynamic stability of oxides is important to predict the atmosphere and temperature in which a material will be sintered. Reaction (1) and Equation (1) shows the reaction between a metal and oxygen for the formation of an oxide and its standard Gibbs free energy change, respectively:



$$\Delta G^0 = \Delta H^0 - T \cdot \Delta S^0 = -R \cdot T \cdot \ln(K) \quad (1)$$

where R stands for the molar gas constant, T represents the absolute temperature, K is the equilibrium constant, ΔH^0 is the standard enthalpy change and ΔS^0 is the standard entropy change. Since K is expressed as the ratio of the activities of the reaction products to the reactants, the activities of the solid phase may be assumed to be equal to unity and the activity of oxygen can be replaced by the oxygen partial pressure (p_{O_2}). Consequently, the equation (1) can be expressed as equation (2):

$$\Delta G^0 = \Delta H^0 - T \cdot \Delta S^0 = R \cdot T \cdot \ln(p_{O_2}) \quad (2)$$

This equation can be used to plot ΔG° in terms temperature for metal oxide systems as shown in the Ellingham diagram on Figure 5. Richard and Jeffes [49] introduced a p_{O_2} scale to the Ellingham diagram, and thus enabling the possibility to estimate the critical oxygen partial pressure for reducing specific oxides at certain temperatures.

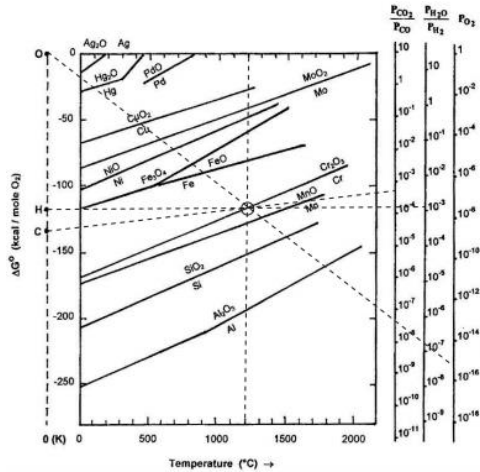
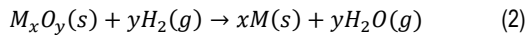


Figure 5 – Ellingham diagram showing the critical values to reduce Cr_2O_3 at $1200^\circ C$ [49].

Also on Figure 5, the p_{H_2O} and p_{CO_2} scales are present, they represent the redox equilibrium expressed by equations (2) and (3).



The equations above fit on predicting oxide stability in relation to pure metals. Although, when Fe alloys are taken into account, computer software calculations [50] should be used since the activity of the elements are lower when than usual due to the fact that alloying elements are in solid solution in the Fe matrix.

Bergman [51] investigated the influence of temperature and partial pressure on the stability of Cr-containing materials. The results showed that the stability of the oxides is shifted to higher oxygen partial pressures when the sintering temperature was raised from 1120 °C to 1250 °C. Figure (6) shows two different oxides thermodynamically stable in steel alloyed with 3% Cr at different temperatures in terms of the p_{O_2} .

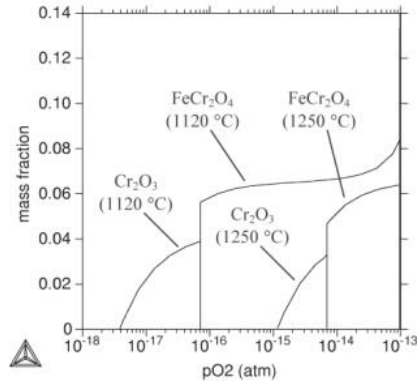


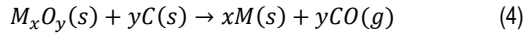
Figure 6 – Mass fraction of stable oxide phases versus oxygen partial pressure for Fe-3%Cr-0,35%C. [51]

Bergman [52] also showed that computer software calculations could also be used to obtain the temperature stability ranges for different oxide phases in a steel at fixed oxygen partial pressure. And by doing so, thermodynamic calculations can be used to obtain the variables necessary to set the sintering process in terms of temperature and oxygen partial pressure in order to create reducing conditions in the processing of oxidation sensitive PM alloys.

Reduction reactions and transport processes inside PM parts should be considered in order to understand how oxides reduce on the powder surface during the sintering.

Reduction of metal oxide during the sintering process can occur through the interaction with H_2 present in the controlled atmosphere according to reaction (2). Carbothermal reduction may occur by the interaction between oxides and carbon

(added in the form of graphite to the powder mix) according to reaction (4). The CO gas generated in reaction (4) may interact with the oxide to cause indirect carbothermal reduction according to reaction (3).



Taking the reactions above into consideration, oxide reductions mechanism in PM powder with 3%Cr-0,5Mo were investigated Danninger et al [53-54] and Hryha [55]. The results indicated that H₂ reduction of iron oxides on the powder surfaces happen in temperatures ranging from 300°C to 600°C during the heating stage in a N₂/H₂ atmosphere. When the temperature of 700°C is achieved, carbothermal reduction is initiated and further iron surface oxide reduction is observed. Intense carbothermal reduction occur when the temperature is above 900°C and thermodynamically stable Cr-rich oxides on the powder surface are reduced. Maximum reduction of these oxides are reached when temperature ranges of 1000-1050°C and 1200-1250°C are reached. Similar oxide reduction sequence was reported by Jalilizyaeian et al [56], but in this research Cr-Mn alloys were investigated and large carbothermal reduction peaks with maximum reduction was achieved at 1250°C due to the removal of stable Cr-Mn oxides.

Liu et al [57] investigated press and sintered stainless steel mixed with graphite and the results also support the fact that effective carbothermal reduction of Cr-rich oxide on powder surface were achieved at the temperature of 1200°C. Sintering was carried out in a vacuum furnace at 1200°C for 30 min and complete reduction of the surface oxides was achieved. Gruner [58] and Berger [59] confirmed this results by heating mixtures of Cr₂O₃ powder and graphite in streaming helium, the reduction started at temperatures of 1000°C and maximum reduction rate was achieved at 1150°C, reduction was completed at 1200°C. The previous researches were carried out on specimens with density of 7,0g/cm³, where open porosity was still present enabling the diffusion of gases to activate the reduction reactions. Danninger

et al [60] also carried out investigations sintering high density materials (around $7,5\text{g/cm}^3$) but results showed that reduction in this materials virtually stopped at 1050°C due to the closing of pore channels and thus Cr-Mn-rich oxides remained trapped in the material even when sintering temperature reach 1300°C . Successful reduction of surface oxides during sintering require open porosity so that gas species involved in the reduction process can be transported through the pore system.

3. Experimental Procedure

3.1 Materials, parts and processing

Five materials were selected to be investigated during the first phase of the study. Table 1 and 2 report the codes for each material, measured chemical composition extracted from the data sheet, lubricant, graphite, and green densities.

Table 1 –Chemical composition (data sheet) of the powders from the first part of the project.

| Material | Code | Chemical composition (wt.%) | | | | | |
|-----------------|------|-----------------------------|------|------|-----|------|------|
| | | Cr | Mo | Ni | Si | V | Cu |
| Astaloy CrM | A | 2,93 | 0.49 | | | | |
| Ancorsteel 4300 | B | 1,11 | 0.77 | 1.0 | 0.7 | | |
| Astaloy CrA | C | 1.76 | | 2.03 | | | |
| FeSiVC | D | | | | 0.6 | 0.16 | |
| Distaloy-AE | E | | 0.5 | 4,09 | | | 1.53 |

Table 2 – Amount of graphite, lubricant, and nominal green density of the materials from the first part of the project.

| Material | Code | Graphite (wt.%) | Lubricant HD (wt.%) | ρ_{green} (g/cm ³) |
|-----------------|------|--------------------|------------------------|---|
| Astaloy CrM | A | 0.55 | 0.6 | 7.1 |
| Ancorsteel 4300 | B | 0.6 | 0.6 | 7.1 |
| Astaloy CrA | C | 0.65 | 0.52 | 7.2 |
| FeSiVC | D | 1.1 | 0.6 | 7.0 |
| Distaloy-AE | E | 0.56 | 0.56 | 7.1 |

3. Experimental Procedure

Distaloy AE was chosen as the reference material since it is one of the most commercially used diffusion bonded powders with 4.0% in weight of Ni content in its chemical composition. Astaloy CrM is a prealloyed powder without Ni, FeSiVC is masteralloy mix also without Ni while Ancorsteel 4300 and Astaloy CrA are prealloyed powders with 1.01% and 2.03% of weight of Ni admixed, respectively. The amount of lubricant mixed into the powder was up to 0.6% wt. and the amount of carbon added in the form of graphite was coincidentally up to 1.1% wt. The green density was set on the typical level of the industrial production for each material.

The list of materials tested on the second part of the project with their chemical composition extracted from the data sheet, the amount of lubricant and graphite is shown in table 3 and table 4. Each powder producer provided 1 material that was best suitable for high temperature sintering considering that reference material was still the same as in the first part of the project, Distaloy AE.

Table 3 – Composition of the powders (from data sheet) of the second part of the project.

| Material | Code | Chemical composition (wt.%) | | | | |
|---------------------------|------|-----------------------------|------|------|-----|------|
| | | Cr | Mo | Ni | Si | Cu |
| Distaloy AE | A | | 0.5 | 4,09 | | 1.53 |
| Astaloy CrM | B | 2,93 | 0.49 | | | |
| Ancorsteel 4300 (Ni-free) | C | 1.11 | 0.77 | | 0.7 | |
| Ecosint A | D | 1.25 | 0.85 | 0.4 | | |

Table 4 - Amount of graphite, lubricant, and nominal green density of the materials of the second part of the project

| Material | Code | Graphite | Lubricant | ρ_{green} |
|---------------------------|------|----------|-----------|-----------------------|
| | | (wt.%) | HD (wt.%) | (g/cm ³) |
| Distaloy AE | A | 0.49 | 0.59 | 7.1 |
| Astaloy CrM | B | 0.45 | 0.63 | 7.1 |
| Ancorsteel 4300 (Ni-free) | C | 0.6 | 0.65 | 7.2 |
| Ecosint A | D | 0,65 | 0.8 | 7.0 |

3. Experimental Procedure

The design chosen for the first part of the study was the ring shape, since the biggest percentage of press & sinter products are axisymmetric and rings are the closest representation of the design of these products. Figure 7 shows a drawing of the ring-shaped specimens.

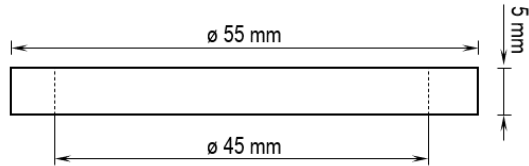


Figure 7 – Drawing of the rings produced.

An industrial hydraulic press was used to manufacture the ring-shaped specimens using all 5 materials. The external diameter (D_{ext}) of the green rings was obtained by using a die with the cavity diameter of $55 \pm 0.005\text{mm}$ while the internal diameter (D_{int}) was manufactured using a core-rod of $45 \pm 0.005\text{mm}$ to create the central hole of the ring.

The compaction strategy used in this case was the double action uniaxial cold compaction, which is the conventional process used in the industry for this type of component.

The design of the components to be tested on the second part of the project was chosen from the portfolio of products of the companies that were partners of the project. In this case, 3 complex shapes were chosen and had their dimensional and geometrical features investigated. The schematic of the design is presented on Figure 8.

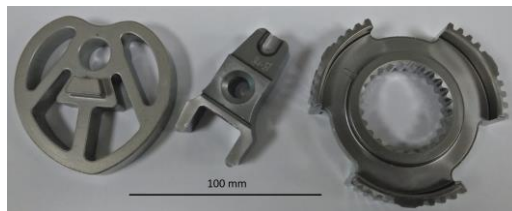


Figure 8 – Design of the 3 complex shapes of the second part of the project.

3. Experimental Procedure

On the first part of the project, 5 materials were separated in 5 batches, each batch was sintered in one furnace at a different temperature. The sintering temperatures were 1120°C, 1180°C, 1250°C and 1260°C, so that it could be possible to investigate the effect of sintering temperature in each material and to compare all the results with the baseline material being sintered at the conventional temperature, 1120°C. The sintering conditions of each furnace were:

- Cremer belt furnace with a sintering temperature set to 1120°C, each batch remained at the sintering temperature for 25-30min with a controlled atmosphere of 90N₂/10H₂ ratio. The cooling rate was of 3.5°C.s⁻¹.
- Cremer belt furnace with a sintering temperature set to 1180°C, each batch remained at the sintering temperature for 25-30min with a controlled atmosphere of 90N₂/10H₂ ratio. The cooling rate was of 3.2°C.s⁻¹.
- Eisenmann roller furnace with a sintering temperature set to 1250°C, each batch remained at the sintering temperature for 25min with a controlled atmosphere of 95N₂/10H₂ ratio. The cooling rate was of 3°C.s⁻¹.
- Eisenmann roller furnace with a sintering temperature set to 1260°C, each batch remained at the sintering temperature for 25min with a controlled atmosphere of 95N₂/5H₂ ratio. The cooling rate was of 3°C.s⁻¹.

The samples were placed onto ceramics plates randomly and introduced into each sintering furnace.

A different amount of either methane or propane was added to the sintering atmosphere to avoid decarburization. The quantity of methane or propane added was different for each furnace based on the experience of the company where sintering trials were carried out.

As per the second part of the project, the specimens produced with Distaloy-AE were separated in 3 batches, while the Ancorsteel 4300, Astaloy CrM and Ecosint A were in 2 batches. One of the batches of Distaloy-AE was sintered at 1120°C in a Cremer belt furnace, soaking at the sintering temperature for 30 min with

3. Experimental Procedure

a controlled atmosphere of 95N₂/5H₂ ratio and carbon control gas of C₃H₈ with a flow of 20L/h, the cooling rate was of 3°C.s⁻¹ and tempered for 15min at 180°C in N₂.

The 2 remaining batches of each material of the second part of the project were sintered at different furnaces:

- Riedhammer roller furnace with sintering temperature set to 1250°C, each batch remained at the sintering temperature for 30min with a controlled atmosphere of 95N₂/5H₂ ratio and carbon control gas of C₃H₈ with a flow of 200L/h. The cooling rate was of 3,7°C.s⁻¹. Tempered for 60min at 180°C in air.
- Eisenmann roller furnace with sintering temperature set to 1250°C, each batch remained at the sintering temperature for 30 min with a controlled atmosphere of 90N₂/10H₂ ratio and carbon control gas of C₃H₈ with a flow of 2,4L/h, the cooling rate was of 3°C.s⁻¹. Tempered for 30min at 200°C in air.

- **3.2 Measurement of parts**

The dimensions and geometry of the specimens (green and sintered) were determined using a Coordinate Measuring Machine (CMM) for both phases of the project, which in this case, was a DEA-Hexagon Metrology Global Image 07-07-07. The machine is equipped with a continuous scanning head SP600 Renishaw and was mounted with a 100mm stylus ending with a ruby sphered probe of 2mm diameter. The accuracy of the data depends on the type of measurement that is being performed, which can be point-by-point or scanning. The accuracy of the data is of 3.4/120 µm.s⁻¹ when using point-by-point measurements while 1.7 µm when using the point-by-point measurements according to ISO 10360-4 [61]. The configuration chosen for the measurements of the green and sintered specimens was in accordance with the sample design, the dimensions to be measured, the support and clamping system used.

3. Experimental Procedure

Figure 9 shows the support with the clamping system attached to the CMM working plane, a 3D holder printed in polymer with the same diameter of the rings was added to the upper part of the clamping system to provide stability during the positioning of the samples. The fastening device consists of 2 triangular shaped holders that tighten the specimen from opposite sides considering the fragility of green specimens. The positioning of the part on the support must contemplate the dimensions and geometry to be analysed as well as the direction from which the probe is going to approach the specimen to acquire the data. A good positioning of the specimen will avoid shadowing of important surfaces to be measured and guarantee high stability and a higher quantity of data extracted by the probe when touching it. All specimens were marked so that the exact clamping position and specimens' label could be easily identified even after the sintering process.



Figure 9 – Clamping system with specimen holder.

The software responsible for the movement and acquisition of the data is the PC-Dmis 2018 software suite.

The measurement procedure (routine) is the same for all specimens with the same design. The routine construction involves 2 main parts: alignment and measurement.

3. Experimental Procedure

The alignment procedure consists in identifying the datum reference frames, in the case of ring-shaped specimens, it is formed by the plane with lower flatness and the internal axis of the central hole. The plane with lower flatness is usually the surface in contact with the lower punches during the compaction phase due to the best filling and compaction of the powder when compared to the top surface. The software reconstructs the lower plane and the central hole axis after scanning both surfaces, they are defined by complete circle scans on the surfaces.

The measuring part for this project was performed using two different techniques. On the first, three points were performed on the top and bottom surface and the height was defined as the average of the distance between two opposing points. The external and internal diameters were defined as the average between three different circle scans performed at $H/4$, $H/2$, and $3H/4$. Where H is the nominal height of the rings. On the second technique, two complete circle scans were performed on the top and bottom surfaces, and hence, two fit planes were calculated. The height was defined as the distance between them. Three full circle scans were performed on the central hole and the external surface also at three different heights just like the first technique, however in the second case cylinders were constructed fitting each three surface scans and they defined the internal and external diameters. Figure 10 shows the scans and points performed to obtain the heights, internal and external diameters.

As per the geometrical features, all results derived from the scans and points performed during the measurement phase.

The same routine was used to measure the rings before and after the sintering. A total of seven specimens were measured for each configuration of the experiment.

The routines prepared for the complex designs on the second part of the project follow the same method as the one described above for the rings. Figure 11 shows the specimens clamped on the support and ready to be measured by the CMM machine.

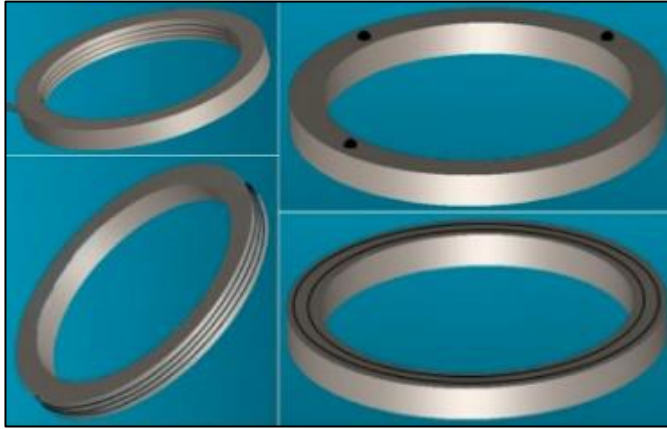


Figure 10 – Scanning and point scans from the CMM schematics.



Figure 11 – Specimens of the second part of the project on the CMM support.

3.3 Density and microstructure

The density of each specimen was measured using the water displacement method as per the ASTM-B962. The porosity was determined from theoretical density, obtained through the mixture rule.

The light optical microscopy (LOM) and the scanning electron microscopy (SEM) were the techniques chosen to perform the microstructural characterization of

3. Experimental Procedure

the specimens, which were etched with Nital 2% regarding FeSiV, Ancorsteel 4300, Astaloy CrA, Astaloy CrM while Picral regarding the Astaloy CrM (on second part of the project), Ancorsteel 4300 (Ni free) , Distaloy AE and Ecosint A. Moreover. The LOM equipment was a Carl Zeiss EL – Einsatz 451887 microscope with a camera attachment using Leica QWin Standard V. 4.0 software, which was also used to obtain images of the porosity of the unetched specimens to analyse the pore morphology. In this case, 4 images of the cross-section with 200x from each specimen were prepared to obtain a total of ~2000 pores and the porosity was processed by image analysis. The software used for this step was the ImageJ, this software can measure each pore separately and provides the information regarding shape and size of it. When the collective information from all pictures is in storage, it is possible to investigate the frequency distribution of the values of each pore characteristics. The median value of the cumulative frequency of 50% of the pores was chosen as the representation of the f_{circle} value for each specimen. Figure 12 shows an example of the filter of the software to identify the porosity where the shape factors will be calculated from.

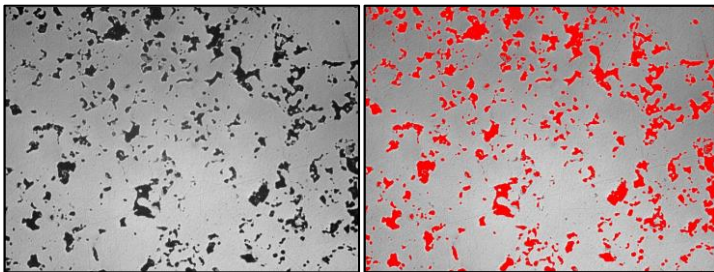


Figure 12 – Image analysis highlighting porosity to be measured.

For this part of the project, the shape factors f_{circle} , f_{shape} and D_{circle} were investigated. D_{circle} represents the diameter of a circle with the same area as the cross section of the pore being investigated. The f_{circle} and f_{shape} values were determined by the equations (3) and (4) respectively:

$$f_{circle} = \frac{4\pi A}{p^2} \quad (3)$$

3. Experimental Procedure

where A and p represent the area and perimeter of each pore identified at the image analysis.

$$f_{shape} = \frac{D_{min}}{D_{max}} \quad (4)$$

where D_{min} and D_{max} stand for the minimum and the maximum Feret diameter.

The f_{circle} and f_{shape} variables represent a morphological characteristic of the smoothness and roundness of the pore surface profile, their value may range from 0 to 1, where 1 stand for a perfect smooth and round surface profile while values close to 0 for a rugged and irregular surface.

The carbon content and oxygen of each specimen was investigated using a Leco Combustion Analyzer and a Leco Inert Gas Fusion Analyser, 6 specimens with 2mm x 6mm x 6mm were cut from the tensile testing parts for each test configuration.

3.4 Mechanical properties

Microhardness, hardness, tensile testing, and impact tests were only performed on the second part of the project.

The microhardness of the specimens was measured using a FM-310 Future-Tech microhardness tester. It was used to describe the microhardness profile from the surface towards the core of the specimens, Vickers indenters with 100g and 1000g was the method used.

The hardness of the specimens was measured using a Emco-Test M4U025 hardness machine also using a Vickers indenter with 10Kg.

Both microhardness and hardness tests were performed on specimens of the impact tests.

Tensile testing using a Instron 8516 machine was performed to obtain the mechanical properties of the specimens (Young's modulus, yield strength, maximum strain, and ultimate tensile strength), the strain rate was 1mm/min. An extensometer with 12mm gauge length was attached to the specimen and it was used to acquire information regarding elongation of the tested part as the force was increased up to

3. Experimental Procedure

the point where fracture occurred. The test and the specimens were prepared as per the ASTM-E8.

Impact tests were performed using an Wolpert PW 30/15 L800mm Impact Machine , 10 unnotched specimens with 10mm x 10mm x 100mm were investigated for each configuration.

4. Results and Discussion

4.1. High Temperature Sintering – Part A

4.1.1. Densification

The results regarding the measurements of the green (ρ_g) and sintered (ρ_s) densities of the tested materials are shown in Figure 13, the density values concerning the cycles with sintering temperatures of 1250 and 1260°C were averaged and represent the highest sintering temperatures of the test.

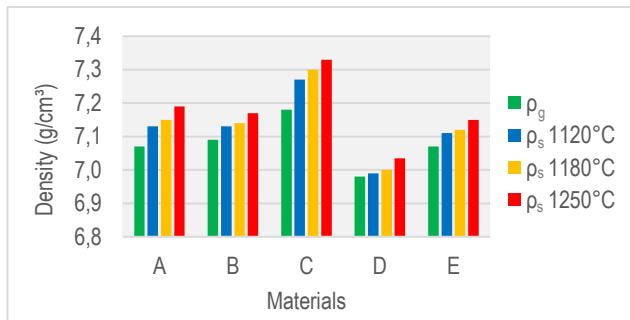


Figure 13 - Green and sintered density of the 5 materials investigated.

The densification parameter can be used to compare the behaviour caused by the rise of the sintering temperature for each material, this parameter is expressed by equation (5),

$$\gamma = \frac{(\rho_s - \rho_g)}{(\rho_{th} - \rho_g)} \quad (5)$$

where ρ_{th} represents the theoretical density.

The values representing γ for the 5 materials under each sintering condition is expressed in Figure 14, where the white filled markers stand for the Ni-free materials while those coloured stand for the nickel containing materials.

All 5 materials present a similar behaviour up to the sintering temperature of 1180°C as the trends are almost parallel to each other. Material D presents a higher densification when compared to the rest of the materials sintered at 1250°C.

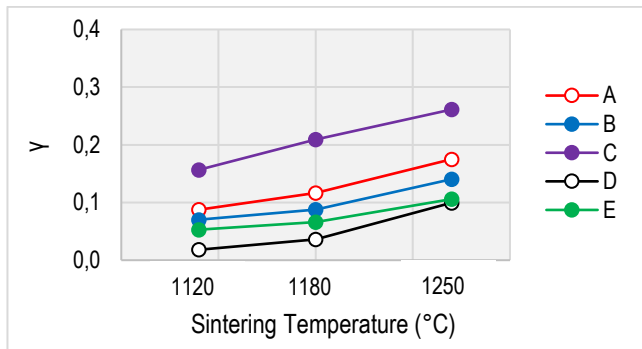


Figure 14 - Densification parameter obtained by eq.(K) as a function of the sintering temperature.

In order to understand the different densification behaviours observed on the tested materials and compare them, it is essential to consider the transformations that guide the shrinkage process during the sintering. Two main factors must be taken into account. The first is caused by the bulk mass transport mechanism, which favours neck growth and hence volume reduction. This effect is increased with the sintering temperature since diffusion also enhances with temperature and it is observable in all five materials. The second factor is connected to the dimensional change caused by the phase transformations occurred during the sintering cycle, mainly guided by the austenite transformation into pearlite/bainite/martensite in the cooling stage. This phenomenon is only observed in the diffusion alloyed materials and is affected by the sintering temperature.

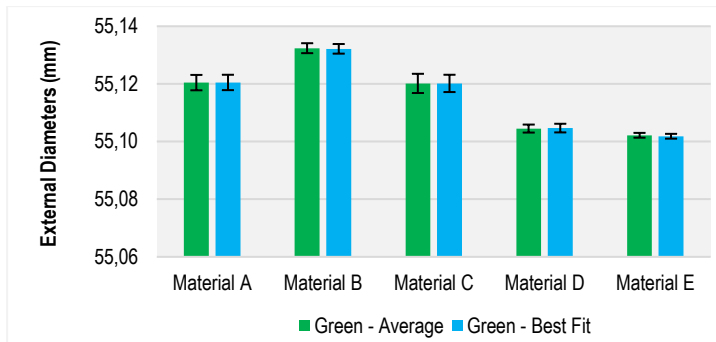
Materials that contain Nickel present better homogenization of the nickel element when the sintering temperature is increased, changing the microstructure

from a highly heterogeneous into to more homogenous microstructure that is a mixture of bainite and martensite, where the ratio of each portion will depend on sintering time, temperature [62]. These phase transformations play an important role on the dimensional changes when sintering diffusion alloyed parts since volume expansion can be observed when perlite turns into bainite an even more when becoming martensite. The transformation of austenite into its different microstructures is somehow increased with temperature.

The microstructures of each material will be deeply discussed further in this work. Nevertheless, the contribution of the phenomena described above should be considered on a different study.

4.1.2. Dimensional measurements

The specimens were measured using different techniques so that the most precise approach could be chosen as standard for the project. The techniques were described in chapter 2 and the results regarding the diameters and height in green rings are presented on Figure 15.



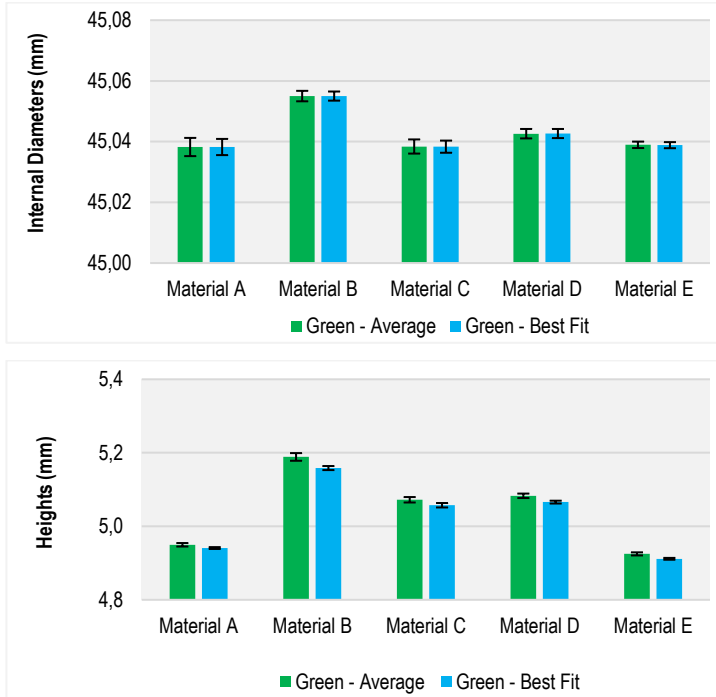


Figure 15 – External diameters, internal diameters and heights of the green rings measured using both average and best fit approaches.

The measurements regarding the diameters showed no difference in terms of the approaches used. The biggest difference observed on the measurement of the diameters was of $0,003 \mu\text{m}$, which is lower than the accuracy of the measuring machine. However, the methods used to measure the heights presented a significant difference of $14 \mu\text{m}$, which can be represented by ISO IT 7 tolerance class. Since the best fit approach obtain several points by scanning the surfaces during the measurement, it is a more accurate representation of the design being studied. So, for this study the best fit approach was chosen as standard procedure.

All the results of the measurements of the diameters and heights regarding the green and sintered specimens are shown in Table 5 and 6. Additionally, the ISO IT tolerance classes was added to confront with the best practices of the PM industry.

4. Results and Discussions

Table 5 – Dimensions of diameters and its respective ISO IT tolerance classes.

| T _{sint} 1120°C | | | | |
|--------------------------|-------------------------------|-------------------------------|-------------------------------|-------------------------------|
| | D _{int,g} / IT class | D _{int,s} / IT class | D _{ext,g} / IT class | D _{ext,s} / IT class |
| A | 45,035 ± 0,004 / 5 | 44,986 ± 0,002 / 3 | 55,120 ± 0,002 / 3 | 55,060 ± 0,003 / 4 |
| B | 45,035 ± 0,000 / 1 | 45,038 ± 0,002 / 3 | 55,132 ± 0,000 / 1 | 55,116 ± 0,003 / 4 |
| C | 45,038 ± 0,002 / 3 | 44,931 ± 0,003 / 4 | 55,121 ± 0,003 / 4 | 54,999 ± 0,005 / 5 |
| D | 45,041 ± 0,001 / 2 | 45,078 ± 0,004 / 5 | 55,105 ± 0,001 / 1 | 55,157 ± 0,005 / 5 |
| E | 45,040 ± 0,001 / 2 | 44,998 ± 0,001 / 2 | 55,102 ± 0,001 / 1 | 55,054 ± 0,002 / 3 |
| T _{sint} 1180°C | | | | |
| | D _{int,g} / IT class | D _{int,s} / IT class | D _{ext,g} / IT class | D _{ext,s} / IT class |
| A | 45,039 ± 0,002 / 3 | 44,933 ± 0,004 / 5 | 55,121 ± 0,004 / 4 | 54,996 ± 0,005 / 5 |
| B | 45,056 ± 0,001 / 2 | 45,027 ± 0,001 / 2 | 55,133 ± 0,002 / 3 | 55,105 ± 0,002 / 3 |
| C | 45,038 ± 0,002 / 3 | 44,880 ± 0,003 / 4 | 55,121 ± 0,003 / 4 | 54,935 ± 0,004 / 4 |
| D | 45,043 ± 0,002 / 3 | 45,027 ± 0,003 / 4 | 55,105 ± 0,001 / 1 | 55,097 ± 0,004 / 4 |
| E | 45,037 ± 0,001 / 2 | 44,970 ± 0,001 / 2 | 55,101 ± 0,001 / 1 | 55,023 ± 0,003 / 4 |
| T _{sint} 1250°C | | | | |
| | D _{int,g} / IT class | D _{int,s} / IT class | D _{ext,g} / IT class | D _{ext,s} / IT class |
| A | 45,041 ± 0,002 / 3 | 44,850 ± 0,005 / 5 | 55,120 ± 0,002 / 3 | 54,896 ± 0,006 / 5 |
| B | 45,054 ± 0,004 / 5 | 44,958 ± 0,003 / 4 | 55,131 ± 0,003 / 4 | 55,022 ± 0,003 / 4 |
| C | 45,039 ± 0,002 / 3 | 44,798 ± 0,002 / 3 | 55,118 ± 0,003 / 4 | 54,837 ± 0,003 / 4 |
| D | 45,044 ± 0,002 / 3 | 44,924 ± 0,005 / 5 | 55,104 ± 0,003 / 4 | 54,971 ± 0,006 / 5 |
| E | 45,039 ± 0,001 / 2 | 44,908 ± 0,003 / 4 | 55,102 ± 0,001 / 1 | 54,947 ± 0,003 / 4 |

4. Results and Discussions

Table 6- Dimensions of heights and its respective ISO IT tolerance classes.

| T _{sint} 1120°C | | |
|--------------------------|---------------------------|---------------------------|
| | H _g / IT class | H _s / IT class |
| A | 4,942 ± 0,002 / 4 | 4,910 ± 0,002 / 4 |
| B | 5,160 ± 0,005 / 7 | 5,132 ± 0,004 / 6 |
| C | 5,065 ± 0,006 / 7 | 5,016 ± 0,013 / 9 |
| D | 5,063 ± 0,001 / 3 | 5,063 ± 0,001 / 3 |
| E | 4,911 ± 0,002 / 4 | 4,897 ± 0,002 / 4 |
| T _{sint} 1180°C | | |
| | H _g / IT class | H _s / IT class |
| A | 4,940 ± 0,002 / 4 | 4,901 ± 0,003 / 6 |
| B | 5,161 ± 0,005 / 7 | 5,128 ± 0,004 / 6 |
| C | 5,055 ± 0,007 / 8 | 5,004 ± 0,007 / 8 |
| D | 5,070 ± 0,006 / 7 | 5,063 ± 0,006 / 7 |
| E | 4,911 ± 0,003 / 6 | 4,893 ± 0,004 / 6 |
| T _{sint} 1250°C | | |
| | H _g / IT class | H _s / IT class |
| A | 4,941 ± 0,002 / 4 | 4,896 ± 0,004 / 6 |
| B | 5,155 ± 0,007 / 8 | 5,116 ± 0,005 / 7 |
| C | 5,052 ± 0,005 / 7 | 4,994 ± 0,005 / 7 |
| D | 5,065 ± 0,005 / 7 | 5,043 ± 0,005 / 7 |
| E | 4,913 ± 0,003 / 6 | 4,891 ± 0,003 / 6 |

The heights and diameters of all specimens decrease after the sintering, nevertheless material D presented an increase after being sintered at 1120°C.

In what concerns the scatter of the measurements, all the results can be considered as low. The green specimens presented a mean scatter of 3 µm for the diameters and 8 µm for the heights while the maximum scatter for the dimensions and heights was of 8 µm and 14 µm, respectively. These results of the diameters match the ISO IT tolerance classes of IT2 and IT4 class for the mean and highest scatter, correspondingly. Moreover, the heights match IT6 and IT7 for the mean and highest scatter values, sequentially.

The tolerance classes highlight how accurate the green parts were manufactured, which later, translated to the sintered specimens. Also, the dimensions

parallel to the compaction plane presented a higher precision when compared to those parallel to the compaction direction.

The same analytic procedure can be used to compare the results after the sintering. So, as reported, the diameters decrease after the sintering and so did the scatter, presenting a mean and maximum value of 6 μm and 11 μm , respectively. As per the heights, the mean values increased to 9 μm and the maximum scatter was of 26 μm . The scatter of the diameters corresponds to ISO IT3 for the mean values and IT5 for the maximum values while regarding the heights they match ISO IT6 and IT8, respectively.

Even though the scatter of the results was increased after the sintering, it should be highlighted that this behaviour was observed only in half of the cases while they either decreased or remained the same after the sintering. When comparing to the best practices of the PM industry, it is possible to indicate that rings presented outstanding results since the conventional tolerance for this type of products is of about IT9-10 and IT11-12 for dimensions perpendicular and parallel to the compaction direction.

Finally, sintering at 1250°C did not affect the scatter of the dimensions.

4.1.3. Dimensional changes

To investigate the shrinkage of these materials regarding the external diameters (ε_{Dext}), internal diameters (ε_{Dint}) and heights (ε_h), the equations (6),(7) and (8) were used, in that order:

$$\varepsilon_{Dext} = \frac{\varepsilon_{Dext,s} - \varepsilon_{Dext,g}}{\varepsilon_{Dext,g}} \quad (6)$$

$$\varepsilon_{Dint} = \frac{\varepsilon_{Dint,s} - \varepsilon_{Dint,g}}{\varepsilon_{Dint,g}} \quad (7)$$

$$\varepsilon_H = \frac{\varepsilon_{Hs} - \varepsilon_{Hg}}{\varepsilon_{Hg}} \quad (8)$$

where *s* stands for the sintered results and *g* for the green ones.

The dimensional changes measured from all materials investigated on the first part of the project are presented on Figure 16.

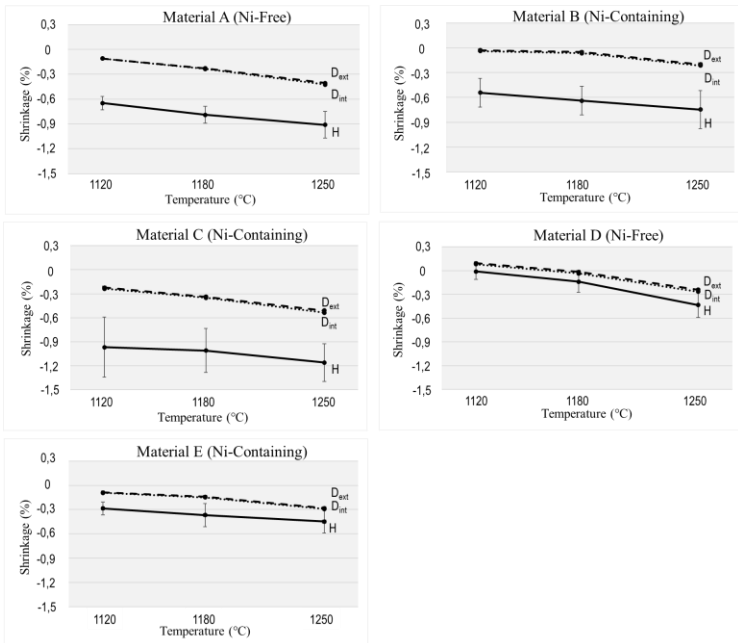


Figure 16 – Dimensional changes of the external diameters, internal diameters and of heights as a function of the sintering process.

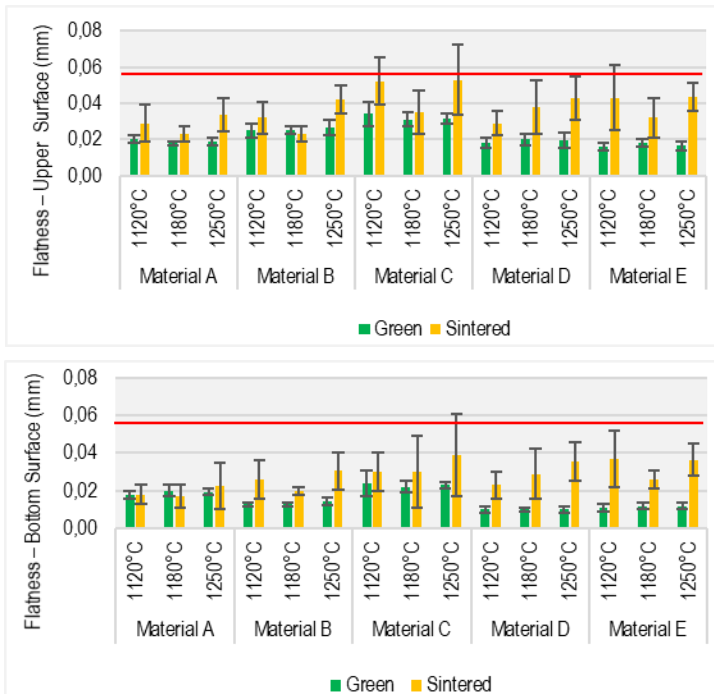
All materials investigated presented similar behaviour in terms of the dimensional changes of diameters. Both external and internal diameters shrink at the same levels. However, shrinkage was anisotropic since heights presented greater shrinkage results when compared to the diameters. Previous studies had already confirmed this anisotropy on the dimensional changes of cold compacted green parts [46]. As per the scatter of the dimensional changes, heights presented greater scatter when compared to diameters. The maximum scatter for the heights was of $\pm 0,3\%$ while for diameters a maximum of $0,02\%$ was obtained. No influence of the sintering temperature was observed.

4.1.4 Geometrical characteristics

The measurements performed on the specimens of the first part of the project were made using the 'best fit' strategy as state on the previous chapter. Taking this into account, all the geometrical characteristics were derived from this data.

The geometrical features investigate were flatness, perpendicularity, parallelism, cylindricity and coaxiality.

The reference data [63] was used to compare the results, generally press and sinter parts should present 0.001D and 0.002D for flatness and parallelism, respectively, where D represents the greater dimension of the surface. In this case, the external diameter was used as 'D', leading to a reference value of 0.055mm for flatness and 0.11mm for parallelism. The reference data is represented by a red line while the flatness and parallelism results are shown in Figure 17.



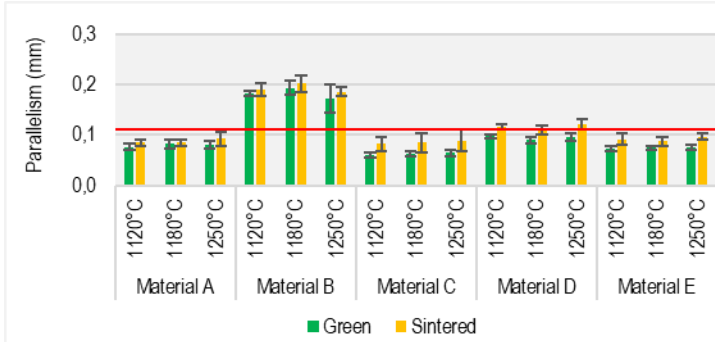


Figure 17 – Upper surface flatness, lower surface flatness and parallelism results with reference data.

Both the flatness of the upper and lower surface presented a similar behaviour, where flatness slightly increases when sintered. Additionally, the scatter of the results is greater when compared to the green specimens. Flatness values increased more when sintered at 1250°C and hence the highest results were obtained from the specimens sintered at the highest temperature. Even though the flatness increased with sintering, all results remained lower than the reference data and no effect of the sintering temperature was observed.

The behaviour of the flatness results was followed by the parallelism. The values slightly increased after the sintering and increased a little more when sintered at 1250°C. Material B presented an abnormal result when compared to the other materials, where its parallelism results were higher than the reference data by an expressive amount already in the green state and thus on the sintered state as well. However, material D also presented values higher but very close to the reference line for the specimens sintered 1120°C and 1250°C.

To clarify behaviour of the results obtained by measuring material B, a comparison between the scans performed in material B and C (which presented low parallelism) are shown in Figure 18, where the scanned points regarding the upper and lower surfaces are presented in a 3d and 2d plot (isometric and side view).

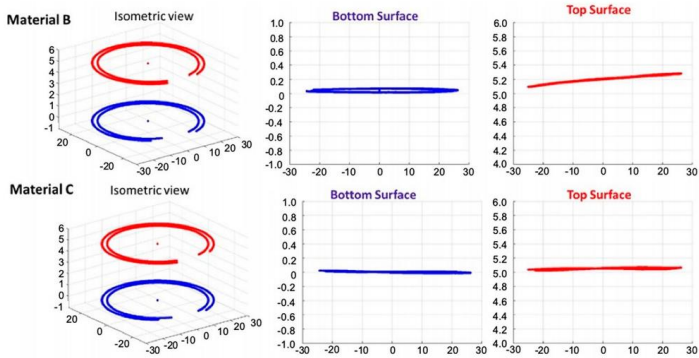
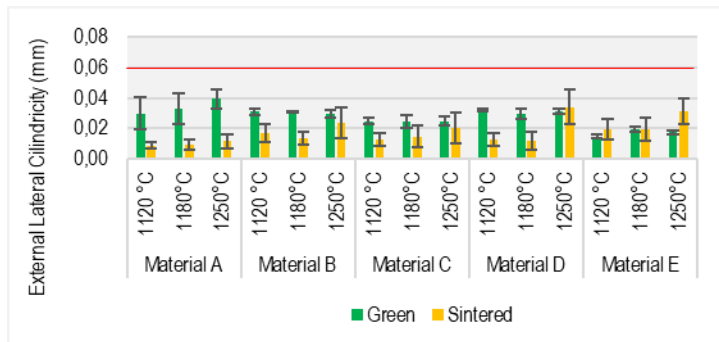


Figure 18 – Scans results of the upper and lower surfaces of the specimens of material B and C.

No anomaly was observed on the bottom surface. However, the top surface results of material B present an inclination that is clearly observed on the side view plot. One of the roots causes of this type of problem is the irregular filling of the die cavity during the production of the specimens. Note that the lower surface does not present this behaviour and therefore it was used as the reference plane to determine all dimensional and geometrical measurements of this study. The results regarding parallelism are mostly defined in the green state, since the influence of the sintering process is very small, the sintered state results are almost the same.

Figure 19 shows the results of the cylindricity and coaxiality of the external and internal lateral surfaces.



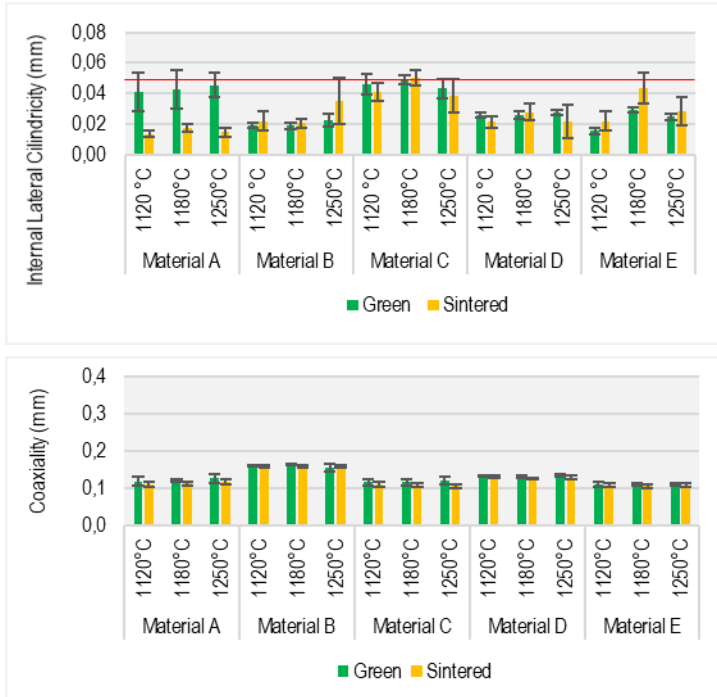


Figure 19 – External lateral cylindricity, internal lateral cylindricity and coaxiality of the cylindrical surfaces.

Again, in this case the reference data with the typical values of the industry are defined as the IT8-IT10 tolerance classes in terms of the internal and external diameters. The highest values of the reference data are plotted in each figure, they are 0,02-0,05mm for the internal lateral surface and 0,023-0,06mm for the external one. No reference data was found in the literature regarding coaxiality.

The cylindricity results do not increase after sintering. In many cases it is observed a decrease in cylindricity and in few cases the scatter band of the green and sintered specimens surpass the reference line. The sintering temperature has no effect on the cylindricity results.

As per the coaxiality of the rings measured, neither the sintering nor the sintering temperature has any significant influence on the results, since the mean values and the scatter band of the measured parts was practically the same for the

4. Results and Discussions

green and sintered specimens. The coaxiality results were therefore defined by the cold compaction.

The results of the external and internal perpendicularity of the rings are presented in Figure 20, where the datum plane was defined by the lower flat surface of the rings. The reference data for perpendicularity is $0,002H$ where H represents the height of the ring and in this case, it leads to a reference of $0,01$ mm for the external and internal surfaces.

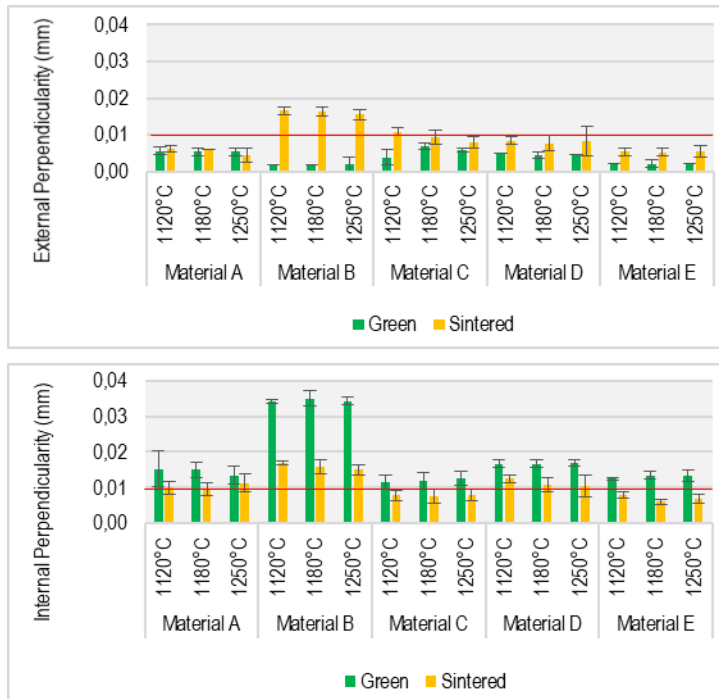


Figure 20 – Perpendicularity of the external and internal cylindrical surfaces in reference to the lower planar surface.

The external perpendicularity increased after the sintering in all cases, except for material A sintered at 1250°C. Regarding the internal perpendicularity, the results after the sintering were lower than in the green state. Material B presented again an unusual behaviour regarding the internal and external perpendicularity,

where the mean values significantly decrease after the sintering in the first case and the opposite occurs to the external perpendicularity. The sintering temperature presented no effect on perpendicularity results. The internal and external perpendicularity presented good results when compared to the reference data for all sintering temperatures.

4.1.5. Microstructure

The unetched microstructure of materials A and B with its respective f_{circle} distribution and cumulative curves for each sintering temperature are presented on Figures 21 and 22. It is important to highlight that the pores observed in the image analysis do not represent single pores, in fact they are part of an extremely complex pore network that is not fully characterized by the shape factors obtained. However, this is currently the best method to describe the pore morphology.

4. Results and Discussions

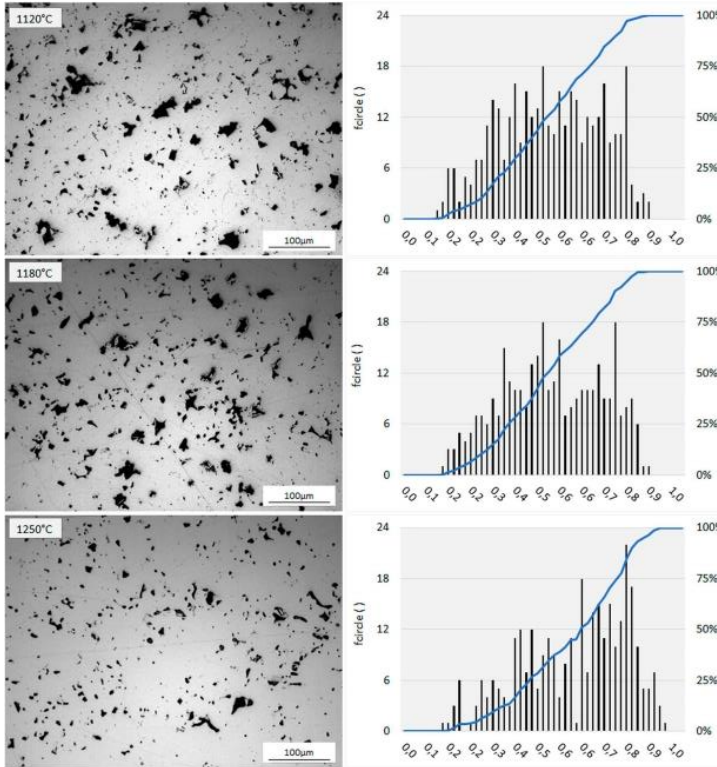


Figure 21 – Uneched microstructure of material A with f_{circle} distribution for all sintering temperatures.

By analysing the f_{circle} distribution graphics, it is possible to observe that the distribution is moving towards one with the increase of temperature [25], as it was previously investigated. This trend is recurrent in all materials studied.

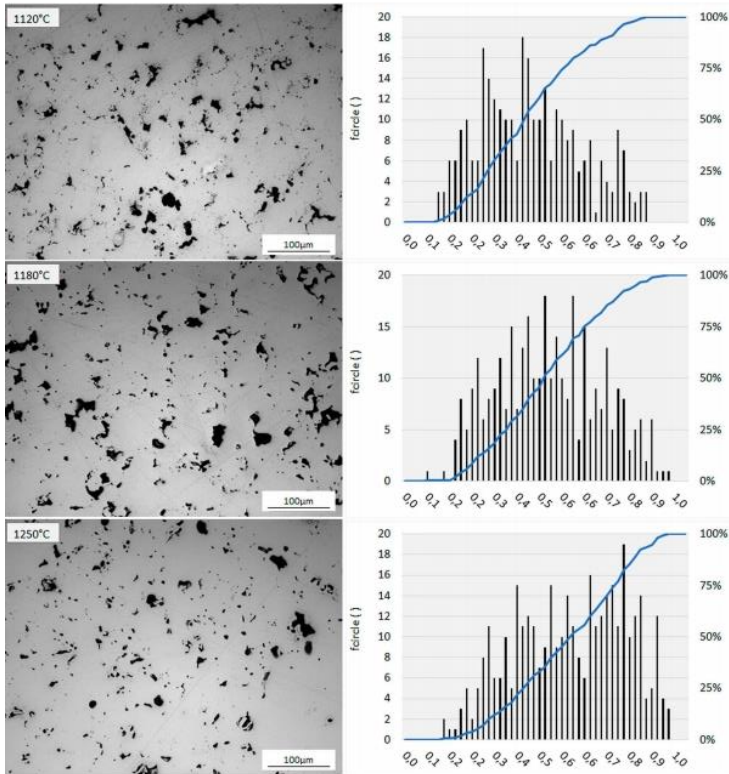


Figure 22 – Unehted microstructure of material A with fcircle distribution for all sintering temperatures.

The shift observed in the distribution refers to the increase in f_{circle} and, of course, the smoothness of the porosity of the material. The f_{circle} median and porosity obtained from each material were used to determine the fraction of the load bearing section Φ using equation (9) [65]. The porosity was determined by using the theoretical densities shown in Table 7 and the densities obtained using the Archimedes method.

4. Results and Discussions

Table 7 – Theoretical densities of all materials tested on the first part of the project.

| Material | Theoretical Density (g/cm ³) |
|-----------------|---|
| Distaloy AE | 7,83 |
| Astaloy CrM | 7,77 |
| Ancorsteel 4300 | 7,65 |
| Astaloy CrA | 7,75 |
| FeSiV | 7,53 |

Table 8 shows the values of porosity (p), f_{circle} and the fraction of the load bearing section for materials sintered at different temperatures.

$$\phi = [1 - (5,58 - 5,57 \times f_{circle}) p]^2 \quad (9)$$

Table 8 – Load bearing section (ϕ), porosity (p) and f_{circle} values for each material investigated.

| Material | A | | | B | | | C | | | D | | | E | | |
|--------------------------------|------|------|------|------|------|------|------|------|------|------|------|------|------|------|------|
| T (°C) | 1120 | 1180 | 1250 | 1120 | 1180 | 1250 | 1120 | 1180 | 1250 | 1120 | 1180 | 1250 | 1120 | 1180 | 1250 |
| p (%) | 8,06 | 7,81 | 7,29 | 6,92 | 6,78 | 6,39 | 6,24 | 5,86 | 5,47 | 7,20 | 7,06 | 6,60 | 9,14 | 9,01 | 8,63 |
| f_{circle} | 0,52 | 0,52 | 0,62 | 0,44 | 0,50 | 0,62 | 0,46 | 0,52 | 0,58 | 0,46 | 0,58 | 0,58 | 0,50 | 0,50 | 0,54 |
| ϕ | 0,62 | 0,63 | 0,72 | 0,62 | 0,66 | 0,76 | 0,66 | 0,72 | 0,77 | 0,62 | 0,70 | 0,72 | 0,56 | 0,57 | 0,61 |

Since porosity decreases while f_{circle} median increases at higher sintering temperatures, the values obtained for the fraction of the load bearing section also increase with sintering temperature for all materials.

Figure 23 shows the values obtained for ϕ for each sintering temperature for both Ni-free and Ni-containing materials.

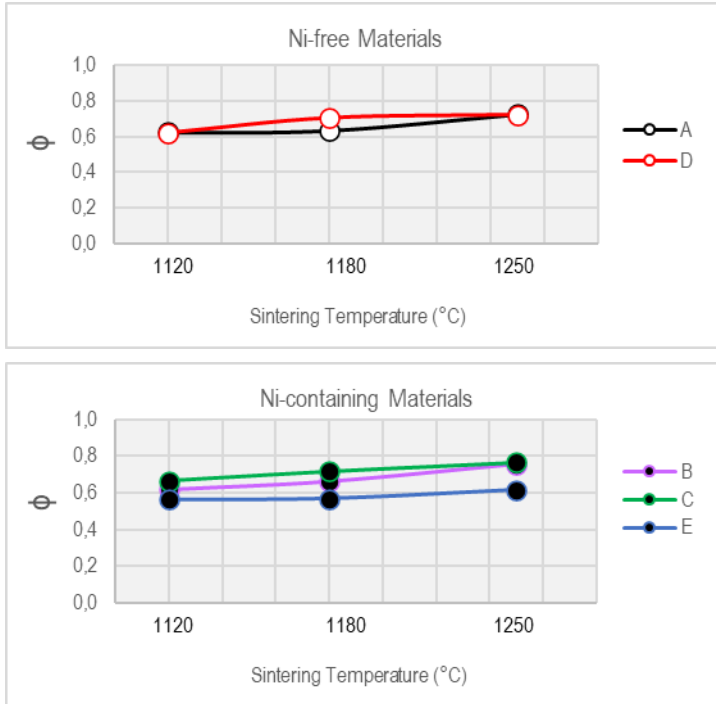


Figure 23 – Fraction of load bearing section in terms of sintering temperatures.

In terms of microstructure of the etched specimens, Figures 24 to 33 shows the images obtained by the LOM and SEM, respectively.

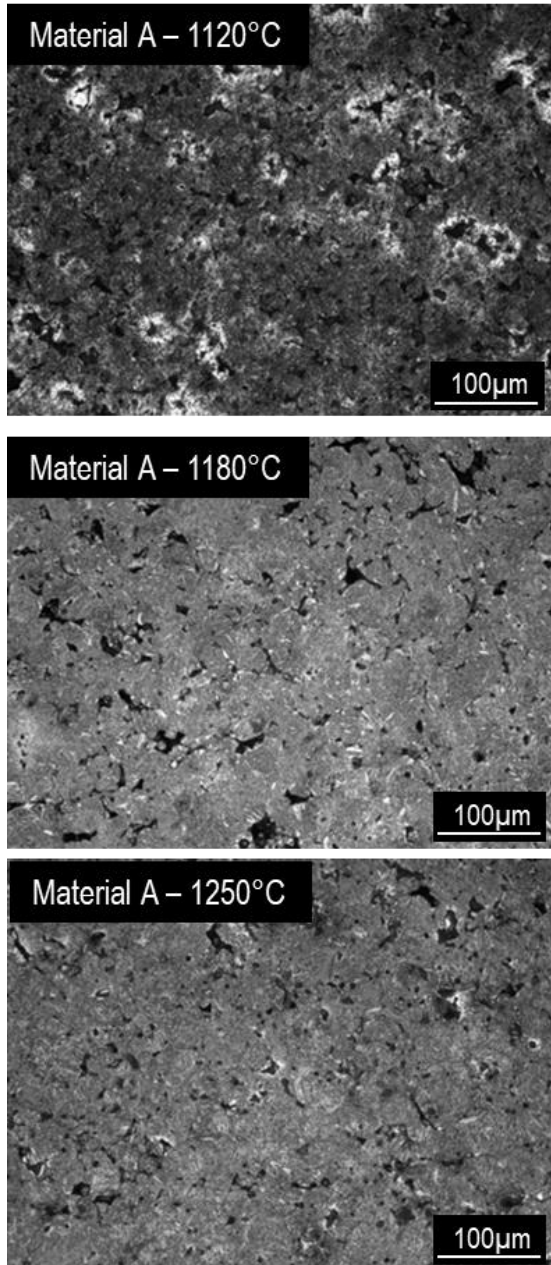


Figure 24 – LOM micrographs of material A at each sintering temperature.

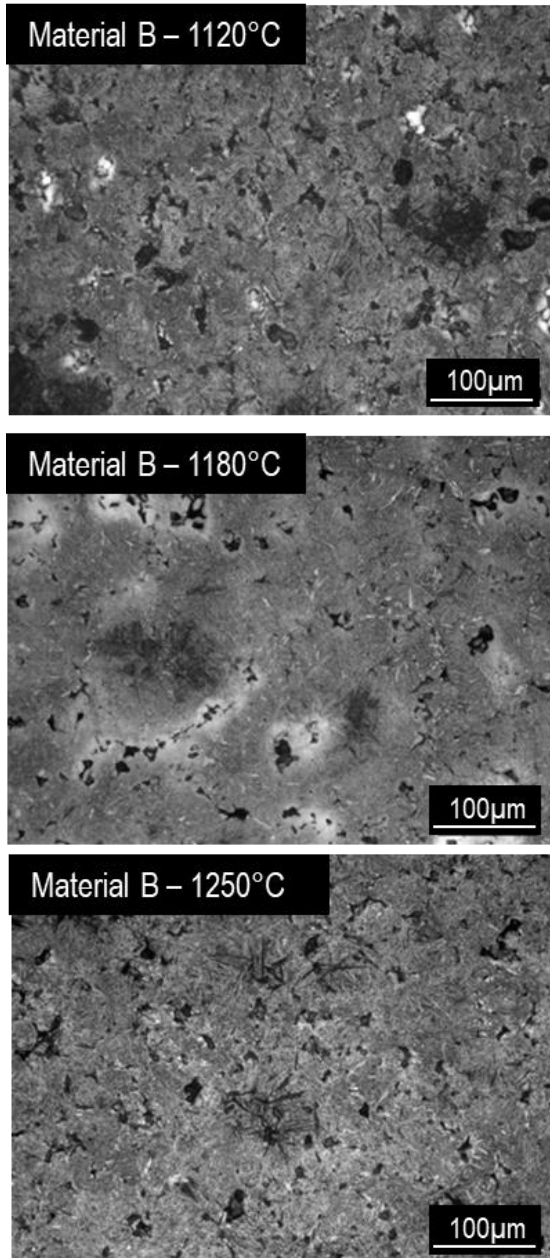


Figure 25 – LOM micrographs of material B at each sintering temperature.

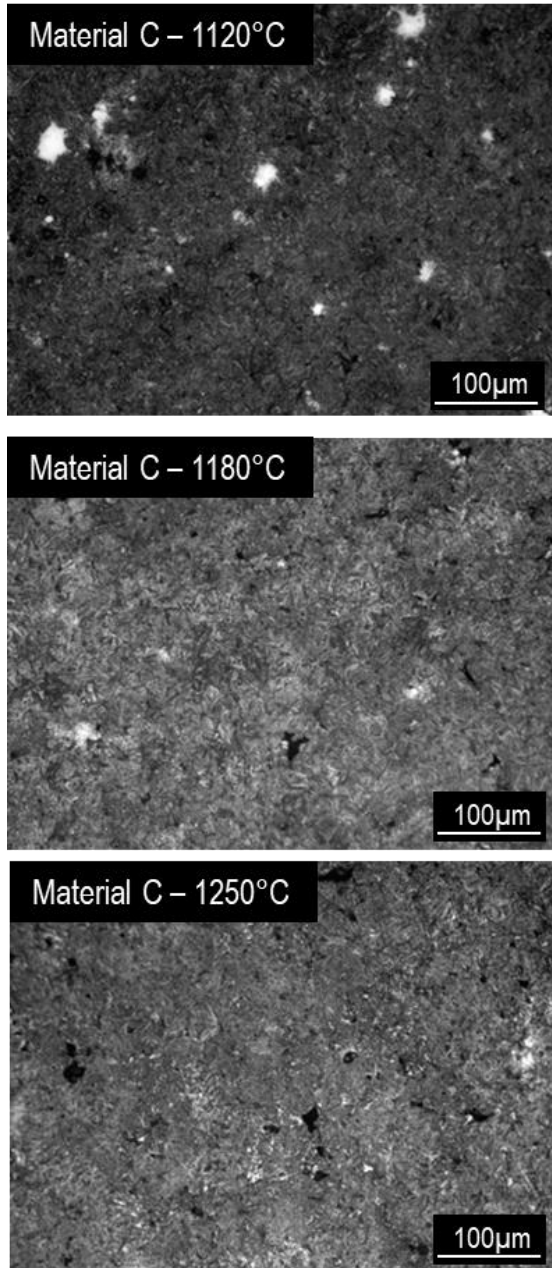


Figure 26 – LOM micrographs of material C at each sintering temperature.

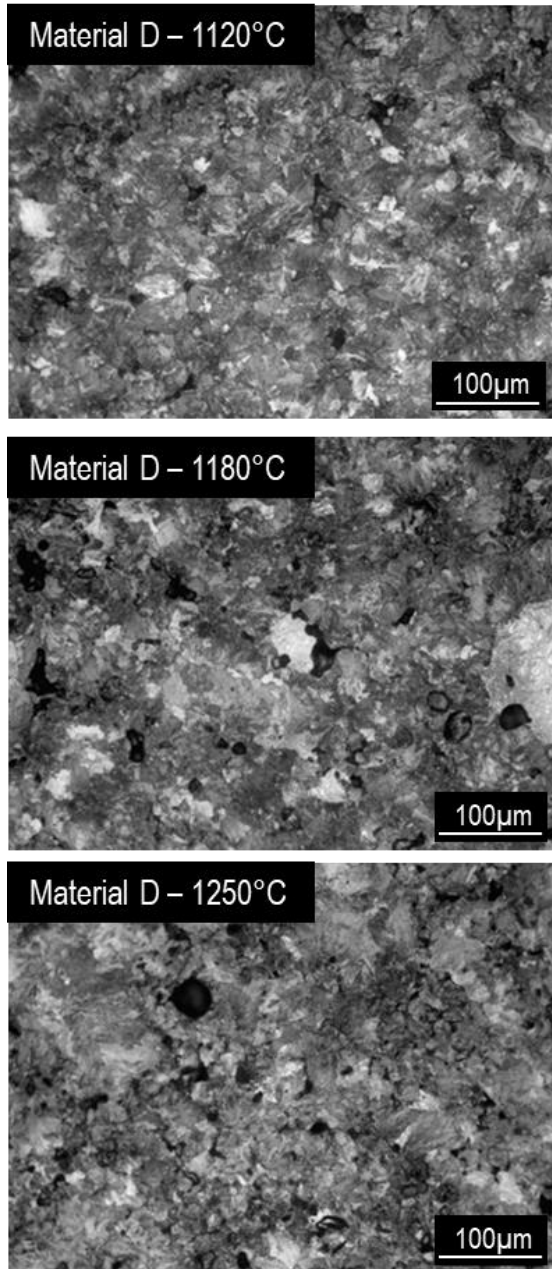


Figure 27 – LOM micrographs of material D at each sintering temperature.

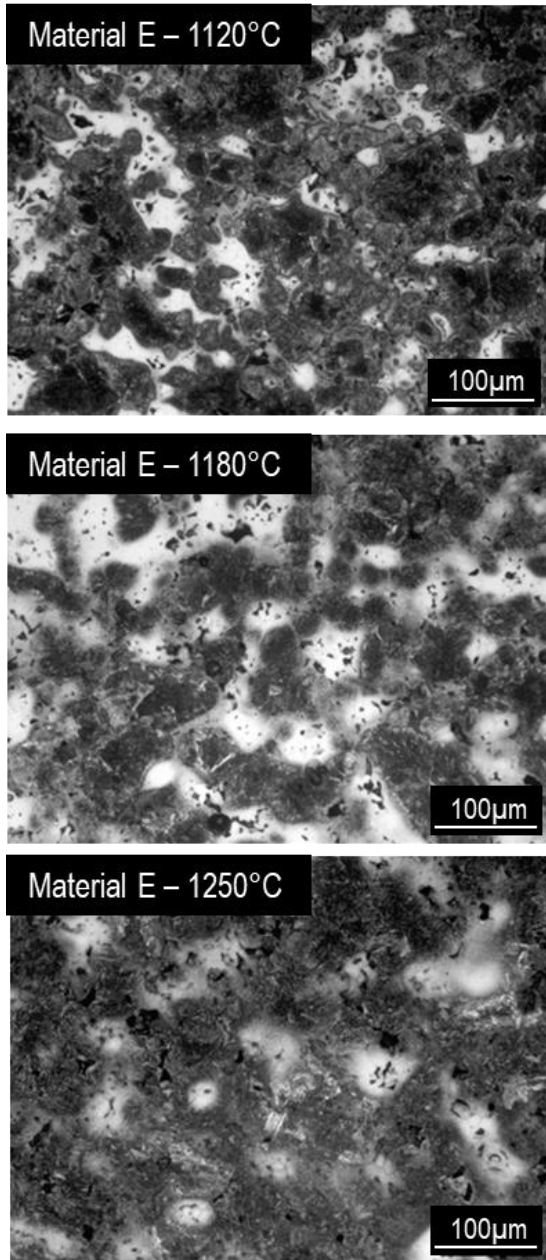


Figure 28 – LOM micrographs of material E at each sintering temperature.

Material A presents a very homogenous martensitic microstructure at all sintering temperatures. The microstructure of material B is a mixture of bainite and martensite at all temperatures. However, some nickel austenite is still possible to be identified at sintering temperatures of 1120 and 1180°C. The same happens with Material C, which presented some nickel austenite at lower sintering temperatures but in a fully martensitic matrix microstructure. Material D by the other hand, presents a very fine pearlitic microstructure, that can be better observed in SEM images. The most heterogenous microstructure can be found in material E, where ferrite, pearlite and martensite are found with the addition of nickel austenitic regions that tend diminish as the sintering temperature is raised. This behaviour is due to the better diffusion of iron into the regions rich in nickel [64]. Additionally, the dissolved nickel causes the increase of bainite and martensite as the amount of pearlitic microstructure decreases. This effect is highlighted by the effect in the hardenability of dissolved Ni in the bulk region of the Ni-containing materials. The microhardness results of all materials are shown in Figure 34, in all cases the microhardness increased with the sintering temperature.

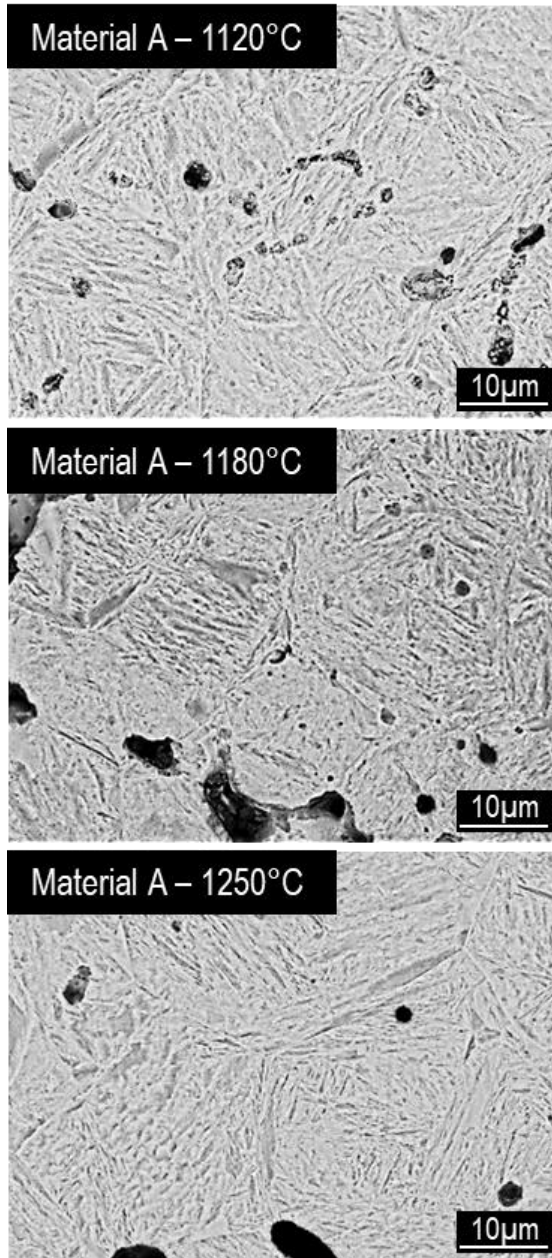


Figure 29 – SEM micrographs of material A at each sintering temperature (1000x).

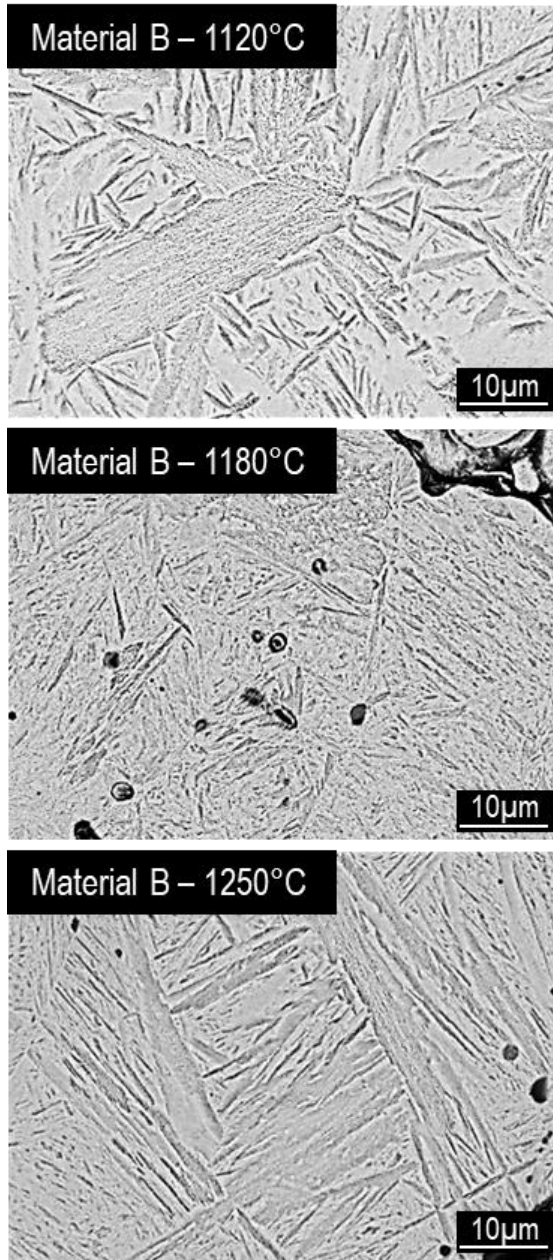


Figure 30 – SEM micrographs of material B at each sintering temperature (1000x).

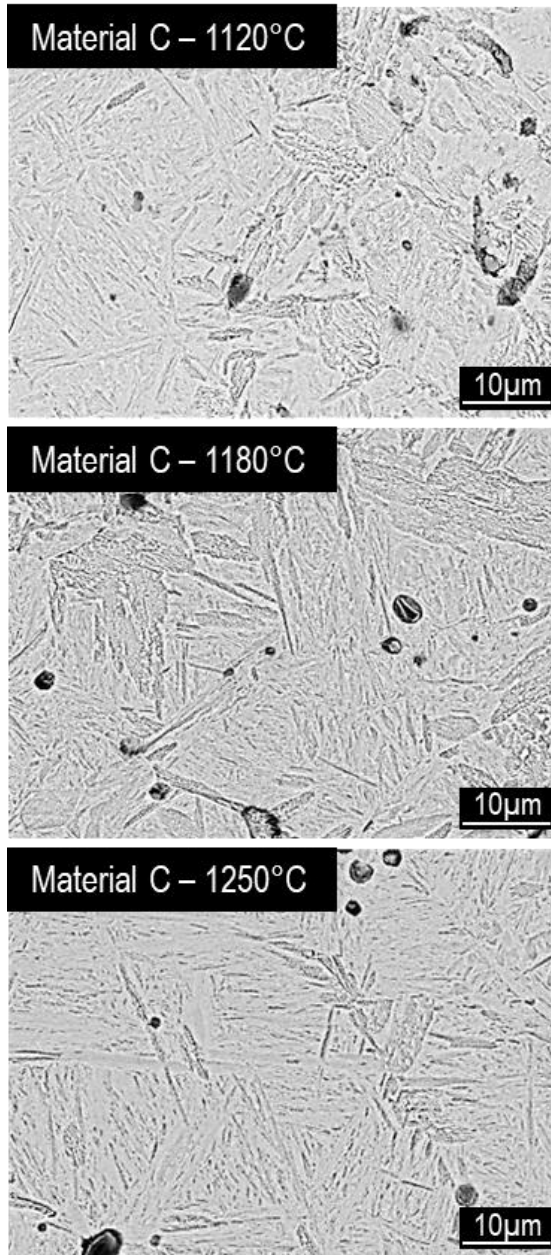


Figure 31 – SEM micrographs of material C at each sintering temperature (1000x).

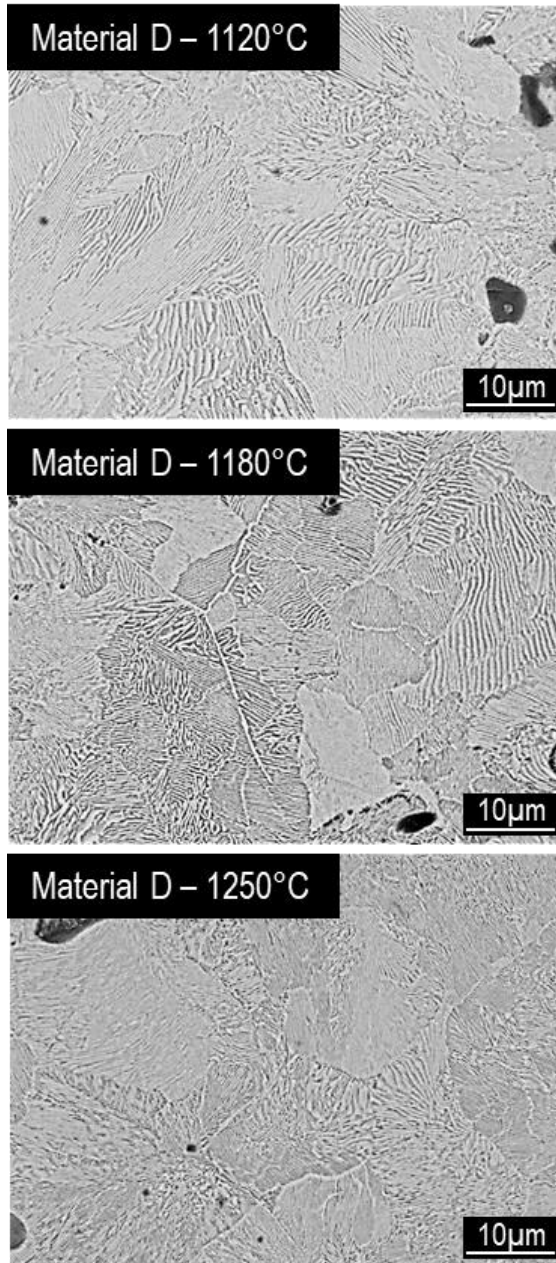


Figure 32 – SEM micrographs of material D at each sintering temperature (1000x).

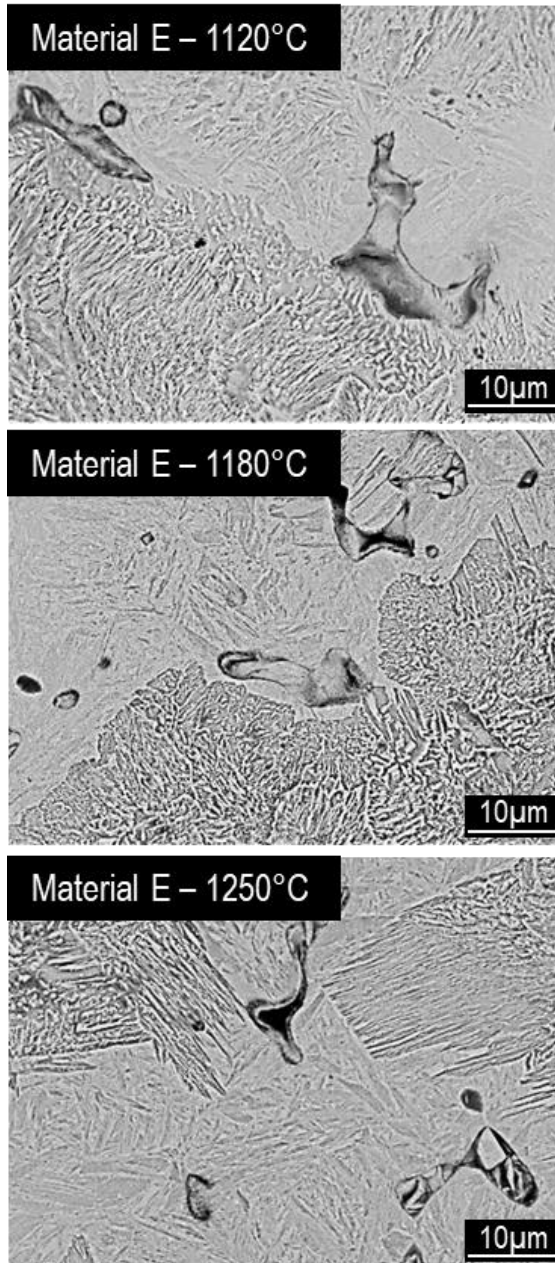


Figure 33 – SEM micrographs of material E at each sintering temperature (1000x).

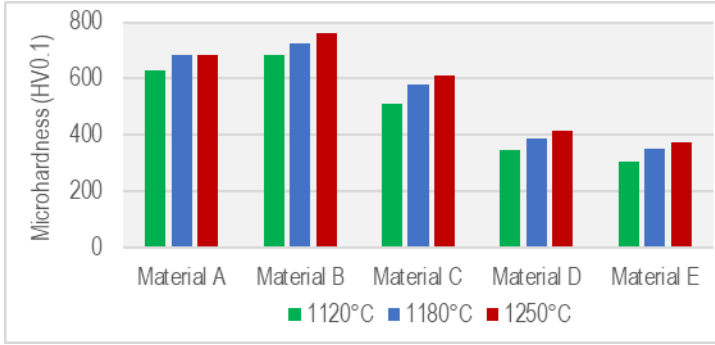


Figure 34 – Bulk microhardness of all materials investigated.

4.1.6. Estimation of the effect of the sintering temperature on mechanical properties

The values of the fraction of the load bearing section can be used to correlate porosity and the pore morphology [65] with mechanical properties using equations (10) and (11) as well as the models proposed by Ashby (12) [66] and Cope (13) [67]. The first two, correlate yield strength (σ) and UTS, respectively. The Ashby model similarly correlate Young's modulus (E) while the Cope model correlates with the tensile elongation (ϵ).

$$\sigma_y = \sigma_{y0} \Phi \quad (10)$$

$$UTS = UTS_0 \Phi \quad (11)$$

$$E = E_0 \sqrt{\Phi} \quad (12)$$

$$\epsilon = \epsilon_0 \Phi^{\frac{3}{2}} \quad (13)$$

where σ_{y0} , UTS_0 , E_0 and ϵ_0 are the relevant properties of the pore-free material or, in other words, of the matrix.

4. Results and Discussions

By using the above equations, it is possible to estimate the increments in each mechanical property as the sintering temperature is risen when compared to the same material sintered at 1120°C. The expected increments on the mechanical properties of each material are reported in Table 9 where the effect of the sintering temperature on the fraction of the load bearing section and hence the mechanical properties is shown. The results of the table below assume that the microstructure of the matrix remains the same even when the sintering temperature is raised, this way the properties of the pore free materials are also the same.

Table 9 – Increments in yield strength (σ_y), tensile elongation (ϵ), UTS, Young's Modulus (E) over the sintering at 1120°C.

| Material | A | | B | | C | | D | | E | |
|------------------|------|------|------|------|------|------|------|------|------|------|
| T (°C) | 1180 | 1250 | 1180 | 1250 | 1180 | 1250 | 1180 | 1250 | 1180 | 1250 |
| σ_y (MPa) | 2% | 16% | 7% | 22% | 8% | 15% | 14% | 17% | 1% | 9% |
| ϵ (%) | 1% | 8% | 3% | 10% | 4% | 7% | 7% | 8% | 0,5% | 4% |
| UTS (MPa) | 2% | 16% | 7% | 22% | 8% | 15% | 14% | 17% | 1% | 9% |
| E (GPa) | 3% | 25% | 11% | 34% | 12% | 24% | 21% | 26% | 1% | 14% |

In a previous research [68], the variations in the mechanical properties were measured and increments of 5-10% were observed in tensile ductility while increments of 20-40% in UTS were measured. All mechanical properties are expected to increase with sintering temperature, but Ni-containing materials might present an extra enhancement in strength and a more discrete increase in ductility due to the evolution of the microstructure, where the Ni rich regions start to disappear as the iron diffuses into the matrix.

4.2. High Temperature Sintering – Part B

4.2.1. Density and porosity

Figure 35 shows the results of the sintered density measurements and the porosity was obtained by using the theoretical density. Table 10 shows the theoretical density of the materials tested on the second part of the project while Figure 36 shows the porosity values.

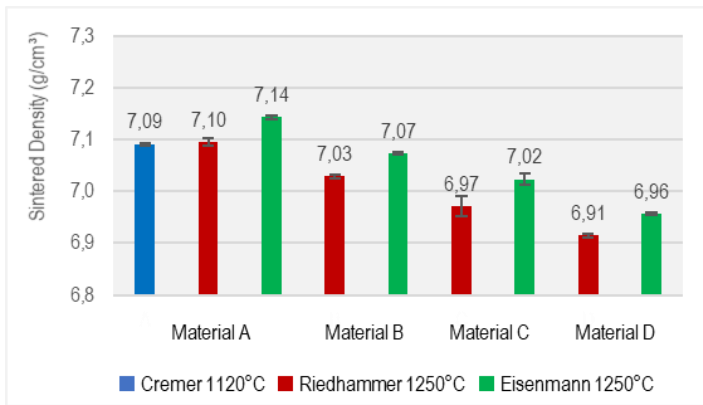


Figure 35 – Sintered density of all materials of the second part of the project.

Table 10 – Theoretical density of the materials of the second part of the project.

| Material | Theoretical Density (g/cm³) |
|---------------------------|-----------------------------|
| Distaloy AE | 7,83 |
| Astaloy CrM | 7,77 |
| Ancorsteel 4300 (Ni free) | 7,67 |
| Ecosint A | 7,77 |

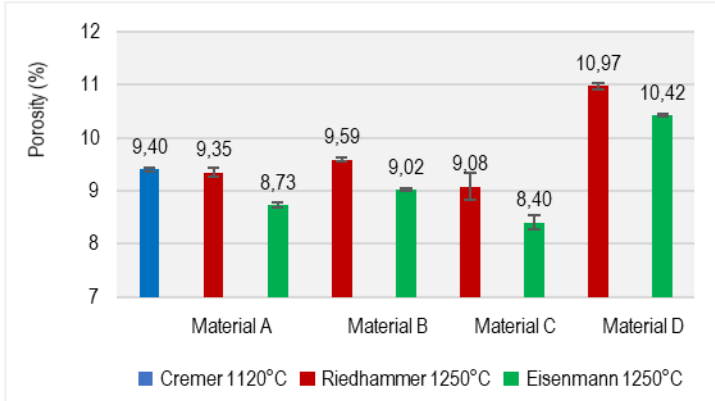


Figure 36 – Porosity of all materials of the second part of the project.

By analysing only the densities of material A, it is possible to observe the influence of the sintering temperature on density between the specimens sintered in the Cremer, Riedhammer and Eisenmann furnace (which present also the highest overall sintered density). The densities from all materials sintered in the Eisenmann furnace were higher than those in the Riedhammer furnace. Material D sintered in the Riedhammer furnace presented the lowest sintered density and higher porosity of all materials.

4.2.2. Dimensional measurements

Although the *modus operandi* chosen to measure the specimens was the same from the previous part of the project, the number of features and surfaces to be analysed increased substantially due to the higher complexity of the shapes studied. For this reason, some of the results are available in the appendix to maintain the coherence of the interpretation of the results.

Figure 37 shows the positions and labels of the dimensions measured in part A.

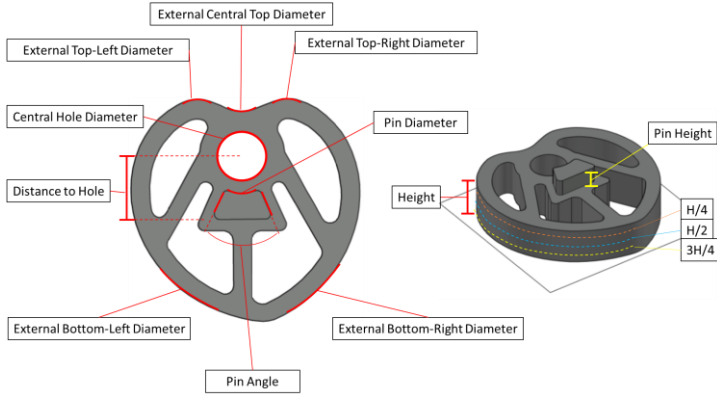


Figure 37 – Dimensions measured from part A.

The results regarding the height and central hole diameter are shown in Figure 38 and 39, correspondingly. The ISO IT tolerance classes corresponding to the scatter of each dimension are reported in the figures.

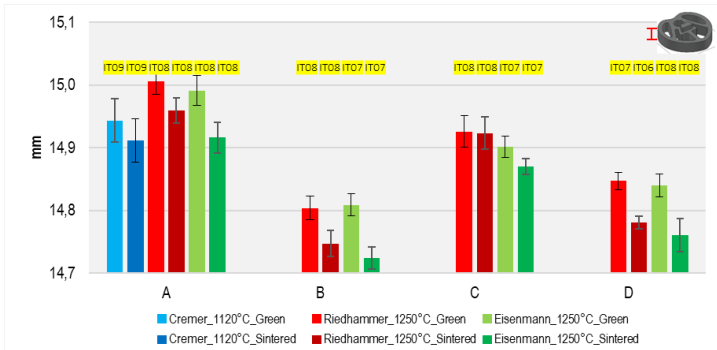


Figure 38 – Dimensional measurements of the heights of all materials.

As expected, the height of the specimens was slightly reduced after the sintering. In terms of ISO IT tolerance classes. The scatter observed in height was the same for green and sintered specimens, except for material D sintered in the Riedhammer furnace. The maximum scatter observed in height for the specimens sintered at high temperature was IT08.

4. Results and Discussions

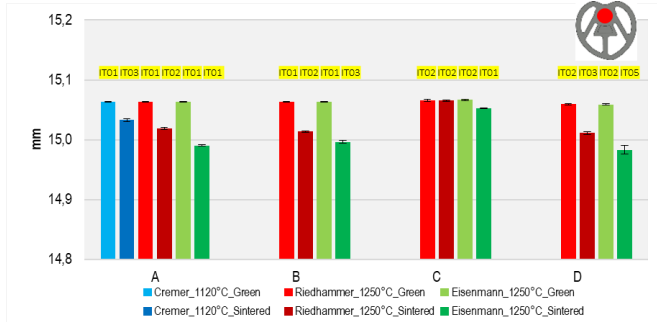


Figure 39 – Dimensional measurements of the central hole diameter of all materials.

As per the central hole diameter, a smaller scatter was observed (maximum of IT05), but again, no influence of high temperature sintering was identified. The precision after sintering was slightly worse than in the green parts. Precision in the compaction plane was higher than in the compaction direction for all materials.

The measurements regarding the pin height and distance to hole dimensions presented high precision (maximum of IT08) while all external diameters and pin angle presented less precision (IT12-IT13). The figures with their respective dimensions are presented in the appendix B of this work. No influence of HTS was observed in the dimensions measured from part A.

The dimensions measured in Part B are shown in Figure 40 with their respective labels.

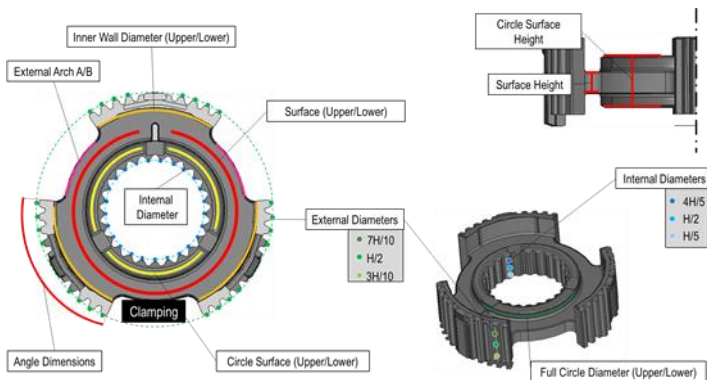
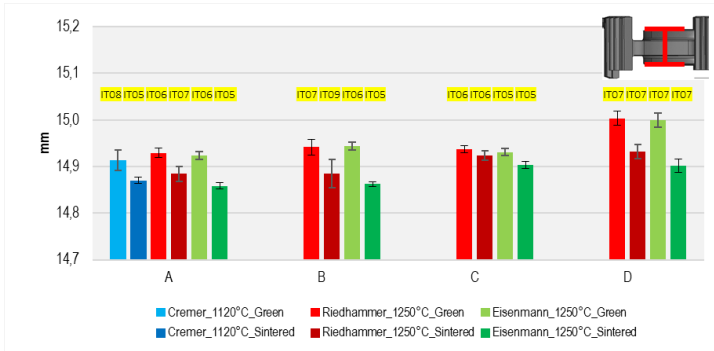


Figure 40 – Dimensions measured and their respective label from part B.

The measurements of circle surface height and inner wall diameter (upper) are presented in Figures 41 and 42, respectively. The upper reference is defined as the surface that interfaces with the upper punch surface while the lower is the surface on the direct opposite side of the specimen.



Figures 41 – Dimensions measured from the circle surface height for all materials.

Dimensions decrease after the sintering while the precision is slightly reduced after the sintering. No clear influence of HTS was observed in the precision of the measurements, this behaviour repeats for the dimensions measured on the compaction direction (refer to the appendix B for the surface height measured).

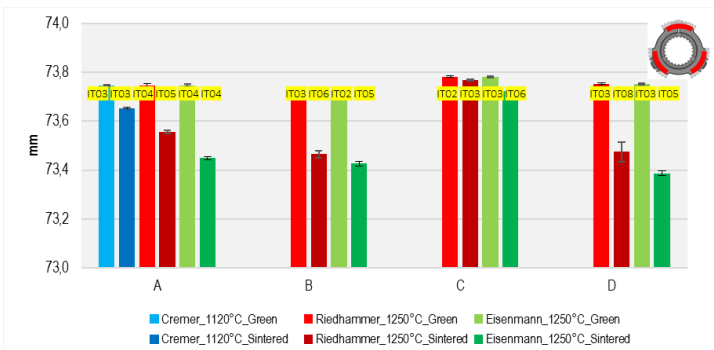


Figure 42 – Dimensions measured from the internal wall diameter (top) for all materials.

By analysing the internal wall diameters, it can be noticed a slightly smaller precision after the sintering. A higher precision can be noticed in the compaction plane than in the compaction direction, except for the lower full circle diameters and external diameters (appendix C) which presented a maximum of IT12. A small effect of high temperature sintering can be noticed in the angle dimensions measured (appendix C).

The internal diameters, internal wall diameters, external arch diameters, heights and full circle diameter of the upper surface presented good precision with a maximum of IT09 after the sintering and no effect of high temperature sintering.

The full list of labels of the measurements performed on the part C is presented in figure 43.

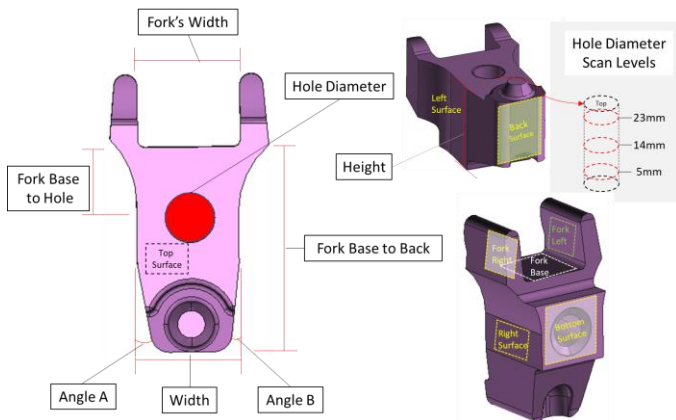


Figure 43 – List of dimensions and labels of the measurements performed in part C.

The measurements regarding the height and width are plotted on figures 44 and 45 as examples of dimensions representing the compaction direction and plane for part C.

4. Results and Discussions

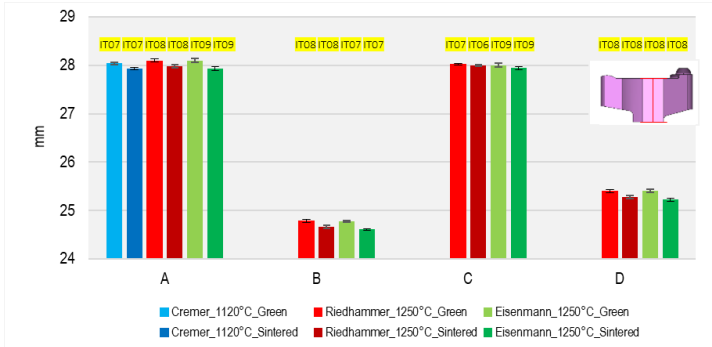


Figure 44 – Measurement of the dimensions of height for all materials of part C.

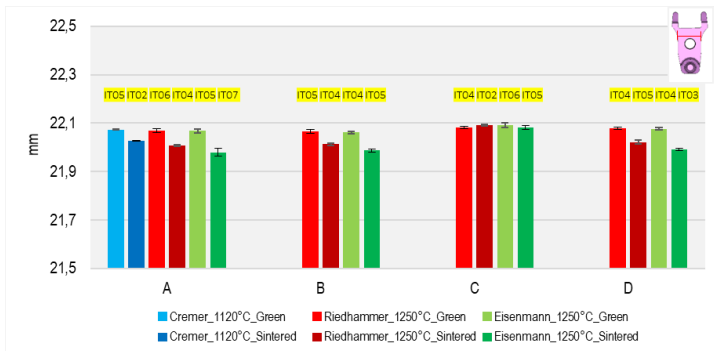


Figure 45 – Measurement of the dimensions of width for all materials of part C.

By comparing the results from figure 44 and 45, it can be noticed a higher precision on the compaction plane when compared to the compaction direction. The only exception from this behaviour were the dimensions from the fork base to hole dimensions and fork base to back dimensions probably due to a distortion caused by the positioning of the specimens inside the transportation packages. The dimensions where the fork base surface was used as reference presented smaller precision with a maximum scatter of IT11.

The hole diameter presented smaller precision after the sintering, while all the other dimensions did not present the same behaviour.

The height, fork's width, hole diameter and the width presented good precision results with a maximum scatter in reference to the ISO IT tolerance classes, the maximum value obtained was of IT09. Also, no effect of HTS was observed.

4.2.3. Dimensional changes

Figure 46 and 47 shows the results from the dimensional changes in the hole diameter and height determined from the dimensional measurements of part A, these figures represent examples of dimensional changes in the compaction plane and compaction direction, respectively. The dimensional changes (ε) for all parts tested were determined by using equation (14).

$$\varepsilon_D = \frac{\varepsilon_{D,s} - \varepsilon_{D,g}}{\varepsilon_{D,g}} \quad (14)$$

Where $\varepsilon_{D,s}$ stands for the dimensions from the sintered state while $\varepsilon_{D,g}$ dimensions from the green state.

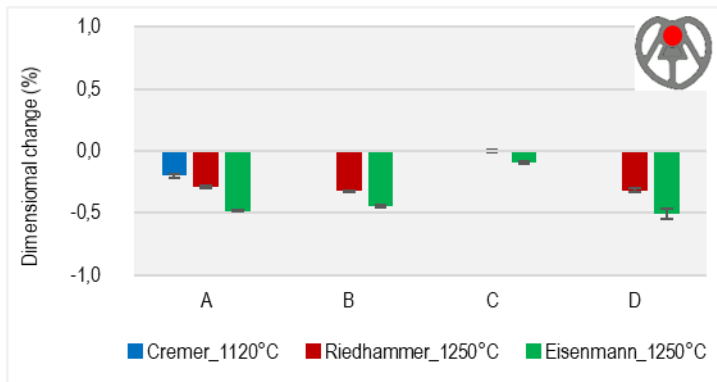


Figure 46 – Dimensional changes in the hole diameter from all materials from part A.

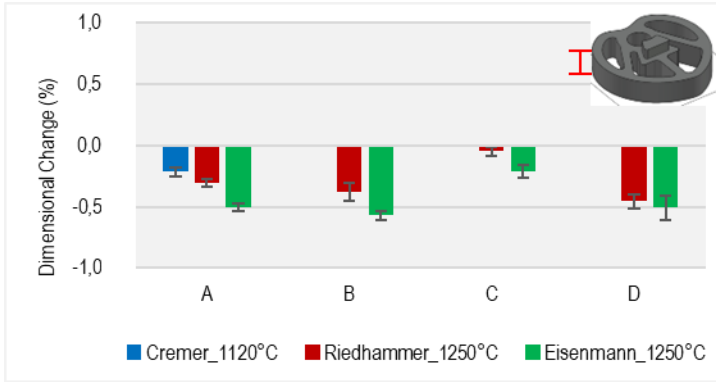


Figure 47 – Dimensional changes in the pin height from all materials from part A.

In both figures it is possible to observe that shrinkage is greater at higher sintering temperatures and even higher after being sintered in the Eisenmann furnace.

Material C presented some swelling (dimensional change above zero) in all measurements besides the external central diameter and height. The other materials shrank after sintering in a very similar behaviour among each other. The external top left diameter, external top right diameter and the pin diameter presented larger scatter than the other results, but they might have been influenced by the measuring instability caused by the lack of references in the CAD model.

The dimensional changes of the surface heights and internal diameters from part B are presented in the Figures 48 and 49.

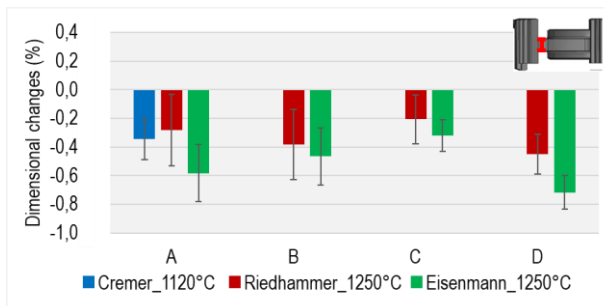


Figure 48 - Dimensional changes in the surface heights from all materials from part B.

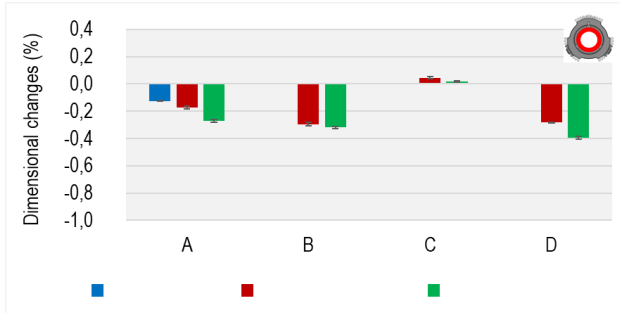


Figure 49 - Dimensional changes in the internal diameters from all materials from part B.

All materials presented a similar shrinkage behaviour besides material C which presented a slight swelling in some cases. The dimensional behaviour is larger in materials sintered at high temperatures and higher in Eisenmann furnace.

The scatter was higher for the full circle diameter (lower surface), external diameter and circle surface height.

Figures 50 and 51 show the results from the dimensional changes of the distance of the hole to fork base and hole diameter, respectively, obtained using the general equation (14) from part C.

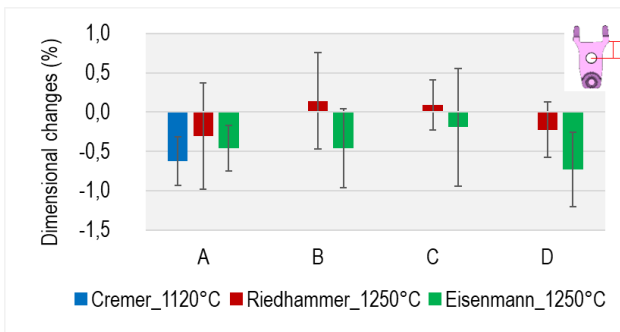


Figure 50 - Dimensional changes in the distance from fork base to hole from all materials from part C

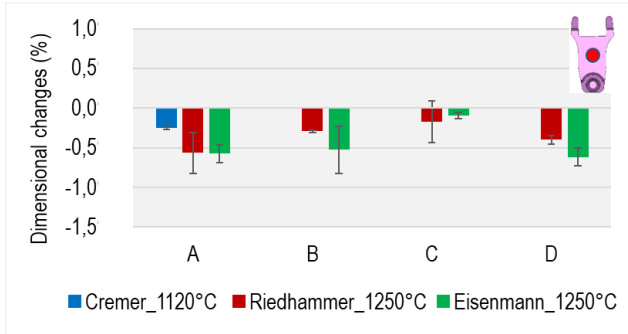


Figure 51 - Dimensional changes in the central hole from all materials from part C

All materials shrink after sintering, besides material C, which presented a swelling behaviour in the hole diameter, width, and distance from fork base to hole dimensions.

Materials presented a slightly larger shrinkage at higher sintering temperatures, but with a similar scatter band. Also, shrinkage was larger in the Eisenmann furnace. A bigger scatter was observed in the hole diameter results and an even bigger one in the fork to hole dimensions.

4.2.3. Geometrical characteristics

The geometrical characteristics were determined from the data from the dimensional measurements. Figure 52 shows the results from parallelism from the top surface, pin surface and perpendicularity of the central hole. The datum plane is highlighted on the drawing attached to each graphic.

4. Results and Discussions

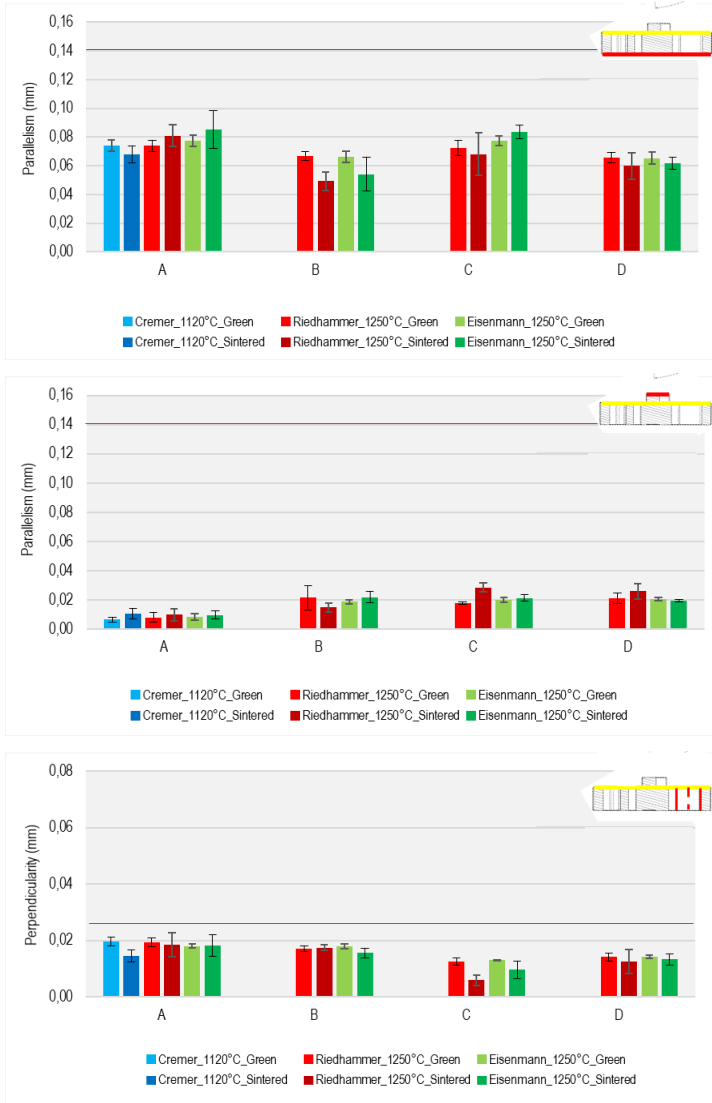


Figure 52 – Parallelism of the top surface, pin surface and the perpendicularity of the central hole for all material of part A.

All the measured geometrical characteristics presented results lower than the references. Additionally, no systematic effect of sintering nor sintering temperature

was observed as the scattered band of the results is stable for all materials and geometrical characteristics for part A.

Part B presented good geometrical results overall as the parallelism of the upper surface shows is Figure 53. Actually, the only geometrical characteristic that surpassed the reference threshold was the flatness of the lower circle surface of part B, presented in Figure 54.

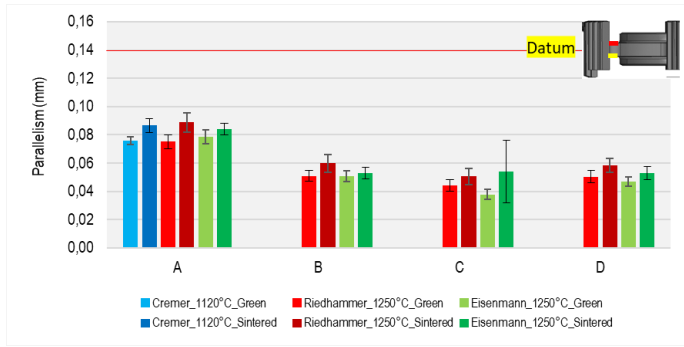


Figure 53 – Parallelism upper surface of all materials tested of part B.

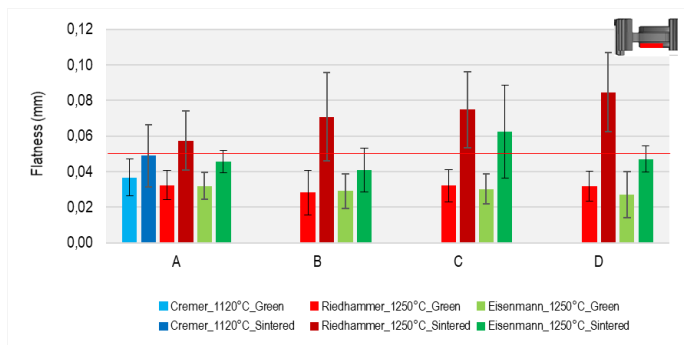


Figure 54 – Flatness of the lower circle surface of all materials tested of part B.

There is clear evidence of a systematic effect of sintering of the part B as the results of the geometrical characteristics tend to be slightly worse after sintering in all cases. However, no effect of the sintering temperature was observed.

4. Results and Discussions

As per part C, the geometrical characteristics determined by the measurements presented good results, except for the flatness of surface in the compaction direction, as shows the flatness of the left surface in Figure 55.

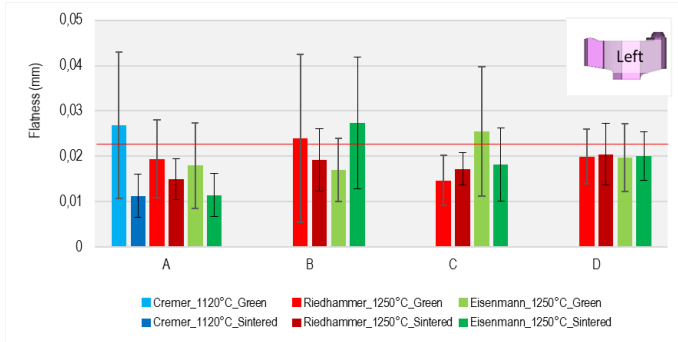


Figure 55 –Flatness of the left surface of all materials of part C.

An example of the good geometrical results found in part C is in Figure 56, where the flatness of the top surface of all materials tested are shown.

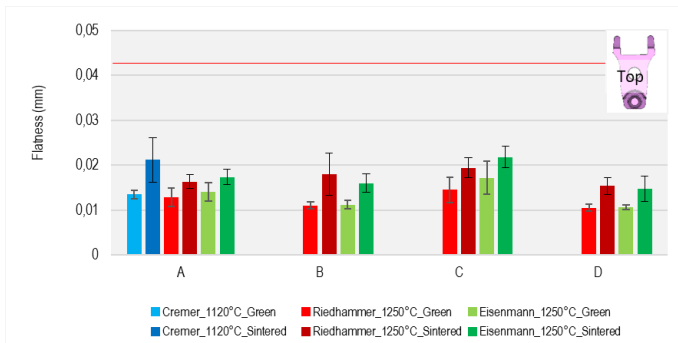


Figure 56 – Flatness of the top surface of all materials of part C.

The systematic effect of the sintering found on part B was also present in a few geometrical characteristics measured in part C as well. And again, no effect of the sintering temperature was observed.

4.2.4. Pore characteristics

Figure 57 shows micrographs of the non-etched specimens of material A sintered at the same temperature (1250°) but in different furnaces, no apparent difference is observed on the porosity or on the morphology of the pores. This behaviour is the same for all materials investigated.

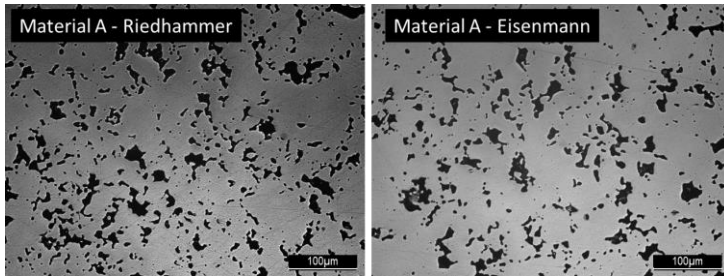


Figure 57 – Micrographs of non-etched specimens of material A sintered using the Riedhammer and Eisenmann furnace.

The pores tend to become rounder as the sintering temperature is raised. Pore morphology is investigated by analysing the f_{circle} values presented in Figure 58. The effect of the sintering temperature is observed in material A, as the values of f_{circle} increase with sintering temperature.

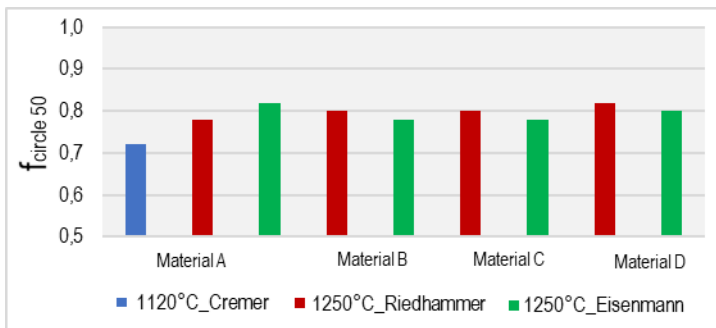


Figure 58 – f_{circle} values of all materials of the second part of the project.

4. Results and Discussions

Materials B,C and D presented f_{circle} values slightly higher when sintered in the Riedhammer furnace.

Figures 59 and 60 present the values of f_{shape} and D_{circle} for all materials investigated, respectively.

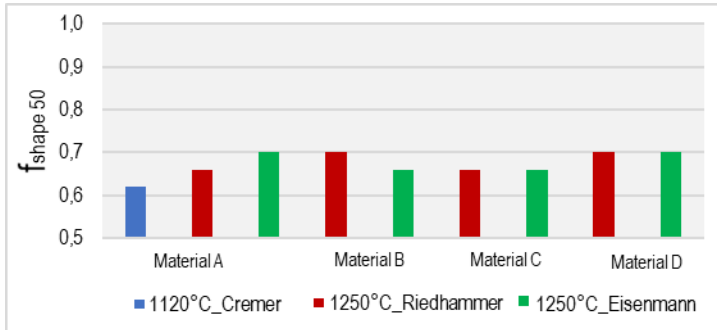


Figure 59 – f_{shape} values for all materials of the part B of the project.

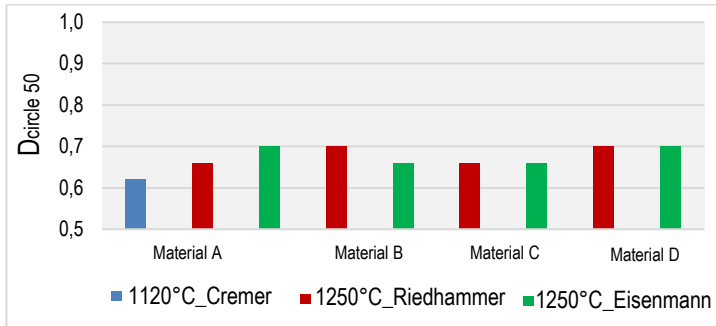


Figure 60 – D_{circle} values for all materials of the part B of the project.

The influence of the sintering temperature is observed on material A on f_{shape} and D_{circle} values. Materials C and D presented the same results for f_{shape} and D_{circle} , while material B showed a small effect of the type of furnace being used. However, the differences between the above parameters for materials sintered at 1250°C in the two furnaces have a poor meaning, since they are relevant to the median of very broad distributions. As a consequence, the one significant effect

observed is the improvement of the pore morphology and the increase in the pore size promoted by sintering at 1250°C demonstrated by the results relevant to material A.

As per the fraction of the load bearing section (ϕ), the results are shown in Figure 61.

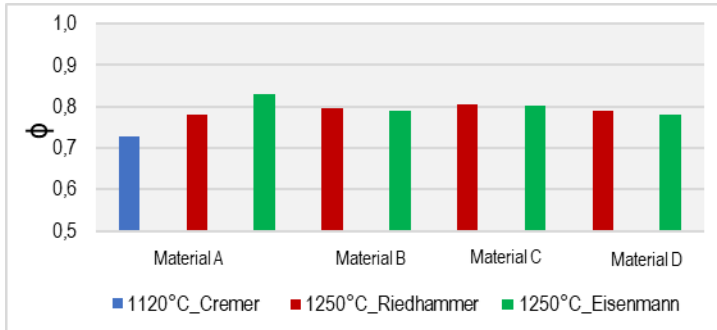


Figure 61 – Fraction of the load bearing section for all materials tested on the second part of the project.

The effect of sintering temperature is highlighted by material A. All the other materials presented very similar results for the fraction of the load bearing section.

4.2.5. Carbon content

The carbon and oxygen content of the specimens was analysed to understand if any decarburization/carburization process occurred during sintering and how it might have affected the microstructure and mechanical properties. Table 11 shows the carbon content added as graphite to the mixture of the powder, the carbon content measured by two of the partners of the project, the average between the 2 measurements and the difference between the carbon content from the mixture and the sintered part as well as the oxygen content.

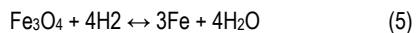
Table 11 – Carbon content mixed in the powder, carbon content after the sintering content of all materials tested.

4. Results and Discussions

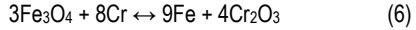
| Material | Temperature | Furnace | C powder | C sintered | C sintered | C sint. | Csint - Cpowder |
|----------|-------------|------------|------------|------------|------------|-----------|-----------------|
| | | | (Graphite) | (MIBA) | (POM) | (average) | |
| | | | % | % | % | % | % |
| A | 1120°C | Cremer | 0,49 | 0,47 | 0,48 | 0,48 | -0,01 |
| A | 1250°C | Riedhammer | 0,49 | 0,43 | 0,45 | 0,44 | -0,05 |
| A | 1250°C | Eisenmann | 0,49 | 0,47 | 0,51 | 0,49 | 0,00 |
| B | 1250°C | Riedhammer | 0,45 | 0,33 | 0,31 | 0,32 | -0,12 |
| B | 1250°C | Eisenmann | 0,45 | 0,37 | 0,39 | 0,38 | -0,07 |
| C | 1250°C | Riedhammer | 0,6 | 0,5 | 0,53 | 0,52 | -0,08 |
| C | 1250°C | Eisenmann | 0,6 | 0,54 | 0,55 | 0,55 | -0,06 |
| D | 1250°C | Riedhammer | 0,65 | 0,37 | 0,4 | 0,39 | -0,27 |
| D | 1250°C | Eisenmann | 0,65 | 0,41 | 0,42 | 0,42 | -0,23 |

The difference between the graphite content of the powder with the carbon content in the sintered parts shows decarburization in high temperature sintered specimens. Material A presented the lowest and even no decarburization in some cases. Material C presented decarburization slightly higher than material A, reaching a maximum of 0,08% in the highest case. Materials B and D showed decarburization values even higher, achieving maximum values of 0,012% and 0,27%, respectively.

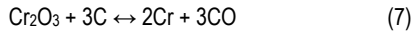
Decarburization is slightly more pronounced in the Riedhammer furnace than in the Eisenmann one. This may be correlated to the lower hydrogen content of the atmosphere (5% vs, 10%, respectively) that plays an important role on the reduction of the oxides on the surface of the particles, in particular in sintering of Cr alloyed ferrous materials. These phenomena have been deeply investigated by Danninger et al. [6]. The particle of a Cr-alloyed powder is covered by a continuous layer of iron oxide with a dispersion of chromium oxide particles. With reference to the main reactions (5) occurring during sintering the interaction between the atmosphere and the powder start at about 500°C when hydrogen reduces the iron oxide:



The higher affinity for oxygen of chromium than iron displays at higher temperature; at about 900°C the following reaction (6) occurs.



That somehow stabilizes oxygen in the material since chromium oxide is much more stable than the iron one. The direct reduction of chromium oxide by hydrogen is unlikely in the industrial sintering atmospheres since it requires a $p_{\text{H}_2}/p_{\text{H}_2\text{O}}$ ratio much higher than that achievable in the industrial furnaces. Chromium oxide may be reduced by the so called carbothermal reduction (7).



That occurs above 1240°C. This reaction is responsible for the reduction of the chromium oxide in the industrial sintering cycles, at the expenses of some decarburization. Considering the sequence of the three reactions above reported, it may be concluded that a higher hydrogen content in the atmosphere enhances the reduction of iron oxide at low temperature, reduces the amount of chromium oxide formed during the final part of the heating step, reduces the extent of the carbothermal reduction and, in turn, decarburization.

Table 11 shows that decarburization increases from steel C to B to D. This trend may be attributed to the different oxygen content of the three powders: 0.12% Ancorsteel, 0.15% CrM, 0.2% Ecosint. It is clear that decarburization increases with the increase in the oxygen content of the powder.

Direct decarburization may be also induced by the difference in the carbon chemical potential between the steel and the atmosphere. The addition of methane and propane opposes direct decarburization, but a comparison between the two sintering cycles that use different carbon control gases and have other structural differences is difficult.

4.2.6. Microstructural analysis

Figure 62 presents the micrographs of the etched specimens of material A made in the light optical microscope.

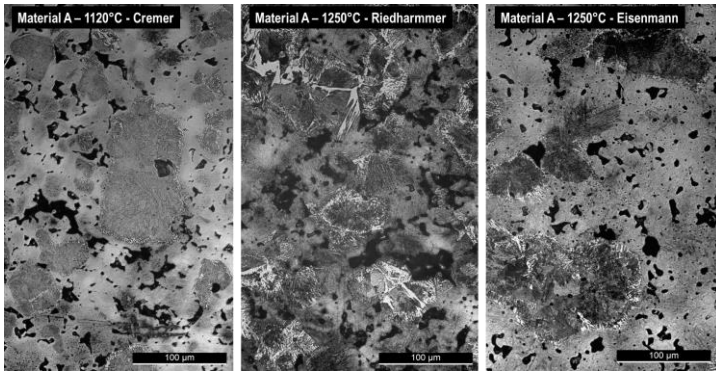


Figure 62 – Microstructure of material A sintered at different temperatures and furnaces.

Material A presents a heterogeneous microstructure of a mixture of pearlite, bainite in a martensite matrix and Ni-austenite. The amount of the Ni-austenite is lower as the sintering temperature is raised since diffusion is enhanced at high temperatures.

Figure 63, 64 and 65 shows the micrographs of the etched specimens of material B, C and D, respectively, both made in the LOM and SEM.

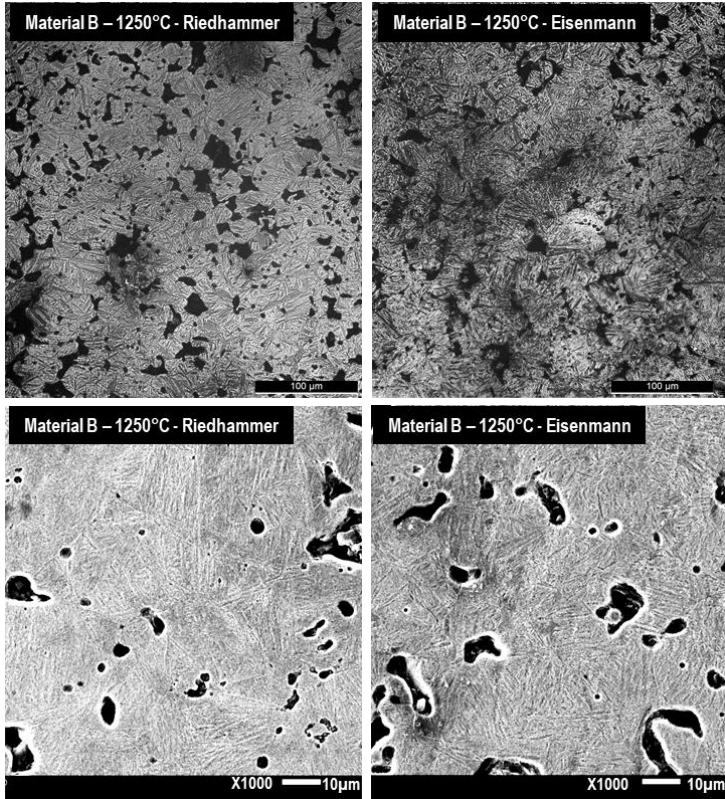


Figure 63 – LOM and SEM micrographs of material B.

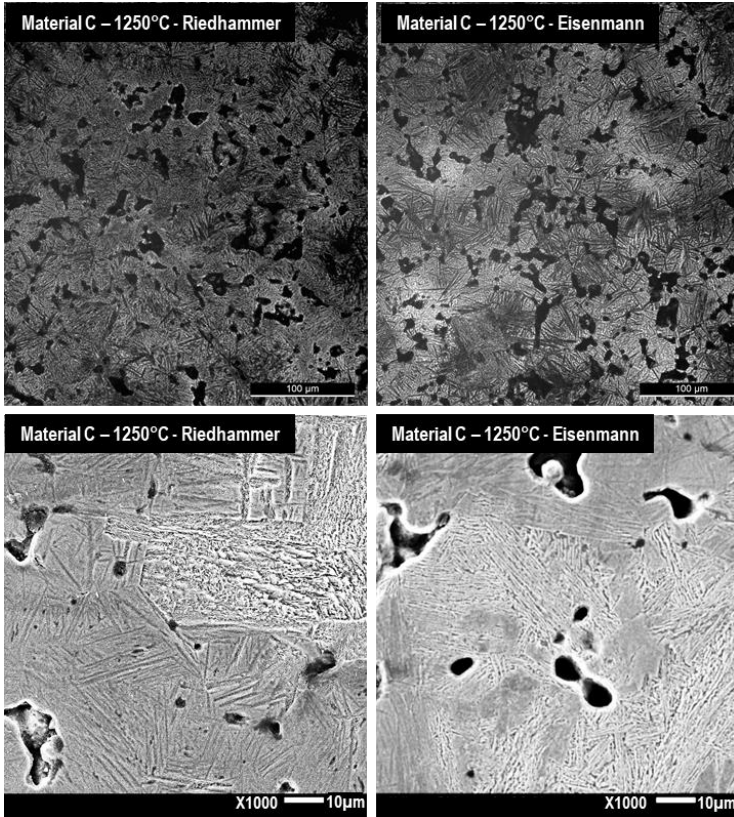


Figure 64 – LOM and SEM micrographs of material C.

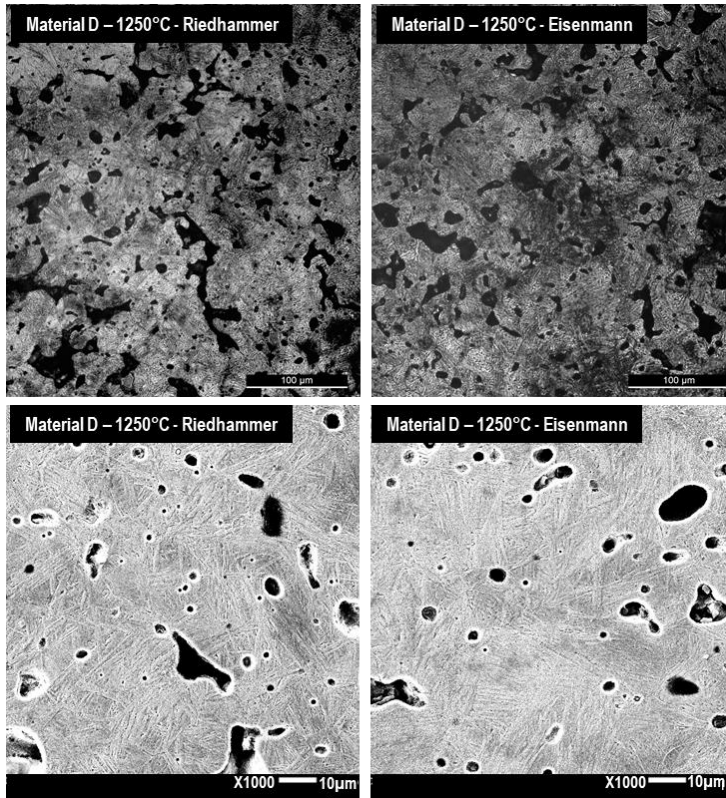


Figure 65 – LOM and SEM micrographs of material D.

The three materials show a martensitic / bainitic microstructure, the amount of bainite is lower in B. To highlight the different amount of the two constituents, colour images were captured at LOM. They are shown in Figures 66 and 67.

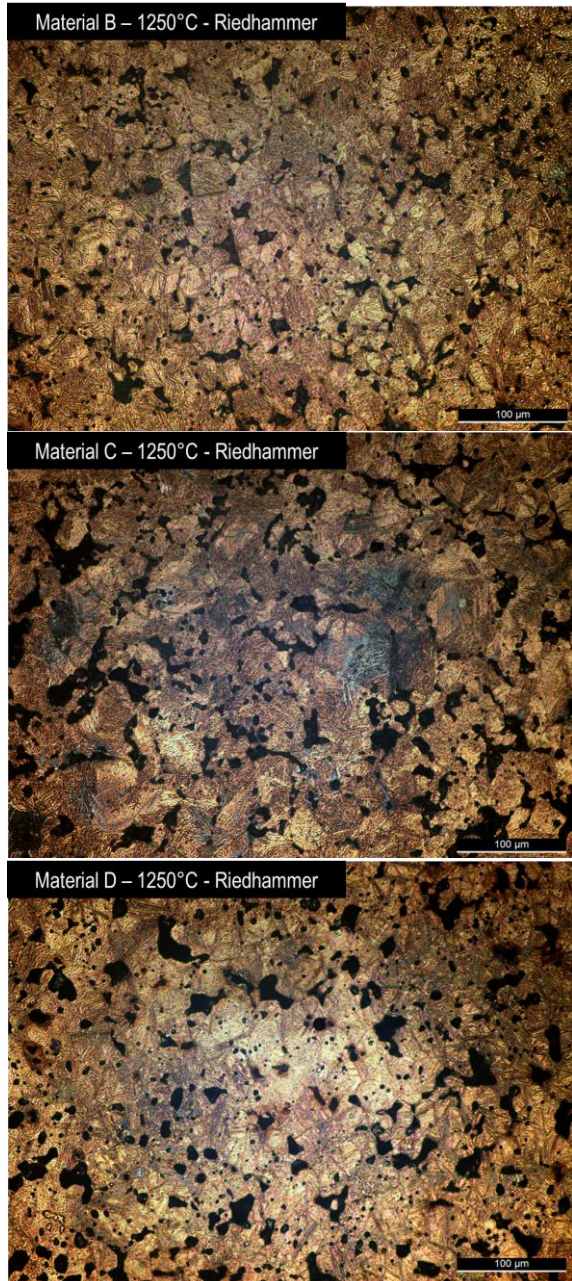


Figure 66 – Color micrographs of materials B, C and D sintered in the Riedhammer furnace.

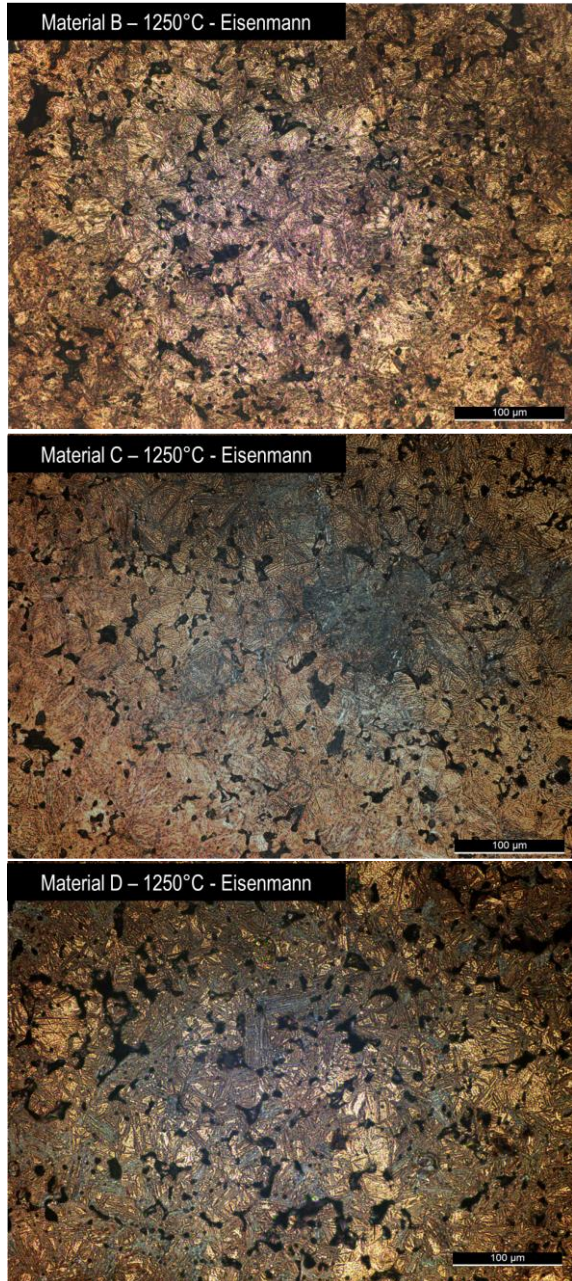


Figure 67 – Color micrographs of materials B, C and D sintered in the Eisenmann furnace.

The amount of bainite is very low and apparently independent on the sintering furnace in material B, while it is higher in the two other materials, in particular in material C and after sintering in the Eisenmann furnace. The differences between the two sintering cycles may be interpreted considering the combined effect of the carbon content and of the cooling rate. The carbon content is higher in the materials sintered in the Eisenmann furnace, while the cooling rate is higher in the sintering cycle performed in the Riedhammer furnace (3.7°C/s vs. 3°C/s). Since the amount of martensite formed on cooling from the sintering temperature increases with the carbon content and the cooling rate, the two sintering cycles do not have a synergetic effect on the formation of martensite. But the differences between carbon contents are significantly different between the three materials, as discussed in the previous section. It is higher in material B and lower in the other two ones. Consequently, it may be hypothesized that in material B the higher cooling rate in Riedhammer furnace compensate for the lower carbon content, and the microstructure is very similar in the materials processed in the two furnaces. In materials C and D, the effect of the higher cooling rate in Riedhammer cycle predominates on that of the small differences between the carbon contents in affecting the austenite transformations on cooling. Therefore, the martensite content of materials sintered in Riedhammer furnace is higher than that of materials sintered in the Eisenmann furnace.

4.2.7. Hardness analysis

Figure 68 presents the hardness measurements performed on the surface (HV0.1, HV1, HV10) and on the cross section (HV1bulk) of the tensile specimens.

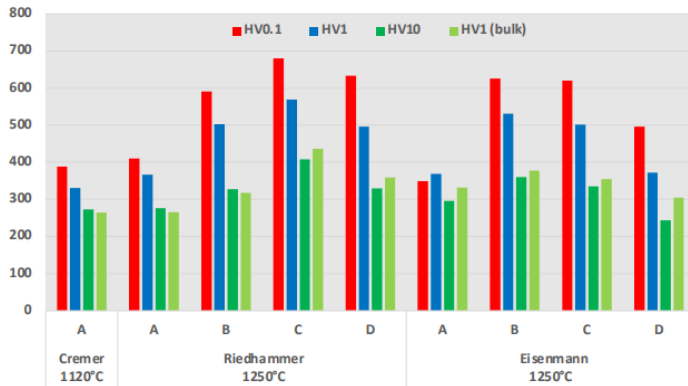


Figure 68 – Hardness measurements of the tensile parts of all materials tested on the second part of the project.

The hardness measured on the surface of tensile specimens decreases on increasing the load, as it may be expected due to the larger volume involved by deformation and, in turn, to the effect of porosity. However, HV1 is higher on the surface than in the bulk, suggesting that carburization might have occurred during the sintering process. Concerning the materials sintered at high temperature, hardness of material B is slightly higher after sintering in the Eisenmann furnace, while that of materials C and D is higher after sintering in the Riedhammer furnace. This result is coherent with the microstructure of the materials discussed in the previous section, even if the microstructural analysis did not highlight a clear difference for material B sintered in the two furnaces. From microhardness and hardness result, it may be concluded that the bainite content is slightly higher in B sintered in the Riedhammer furnace. A further confirmation is provided by the scatter of HV0.1 data, that are not affected by porosity. A larger scatter is indicative of a more heterogeneous microstructure. Scatter is slightly higher for material B in Riedhammer sintering where the scatter was of 86HV while in the Eisenmann sintering it was of 24HV. Materials C and D presented higher scatter in the Eisenmann furnace, the measured scatter was of 49HV and 45HV, respectively, while in the Riedhammer furnace the scatter they were of 13HV and 27HV.

4.2.8. Mechanical properties

The tensile and impact properties of all materials tested on the second part of the project are reported in Table 12.

Table 12 – Tensile and impact properties of the materials tested on the second part of the project.

| Material | Temperature | Furnace | Young's Modulus | | Yield Strength | | UTS | | Elongation | | Impact Resistance | |
|----------|-------------|------------|-----------------|----------|----------------|----------|---------|----------|------------|----------|-------------------|----------|
| | | | Average | σ | Average | σ | Average | σ | Average | σ | Average | σ |
| | | | GPa | | MPa | | MPa | | % | | J | |
| A | 1120°C | Cremer | 136 | 3 | 476 | 11 | 941 | 15 | 3,8 | 0,2 | 29,4 | 2,1 |
| A | 1250°C | Riedhammer | 157 | 7 | 531 | 20 | 1010 | 13 | 3,6 | 0,2 | 30,1 | 2,2 |
| A | 1250°C | Eisenmann | 159 | 7 | 555 | 17 | 1079 | 30 | 3,8 | 0,5 | 33,5 | 1,7 |
| B | 1250°C | Riedhammer | 146 | 6 | 688 | 17 | 1132 | 18 | 2,4 | 0,1 | 23,3 | 1,6 |
| B | 1250°C | Eisenmann | 159 | 8 | 680 | 20 | 1191 | 24 | 2,3 | 0,2 | 23,8 | 2,1 |
| C | 1250°C | Riedhammer | 145 | 12 | 707 | 30 | 1188 | 10 | 1,5 | 0,0 | 18,5 | 1,6 |
| C | 1250°C | Eisenmann | 159 | 7 | 620 | 24 | 1093 | 21 | 2,0 | 0,1 | 19,8 | 1,8 |
| D | 1250°C | Riedhammer | 151 | 12 | 625 | 25 | 1116 | 20 | 2,3 | 0,2 | 23,1 | 1,4 |
| D | 1250°C | Eisenmann | 154 | 13 | 598 | 27 | 1068 | 13 | 2,9 | 0,3 | 26,0 | 0,7 |

Tensile properties are graphically reported in figure 69.

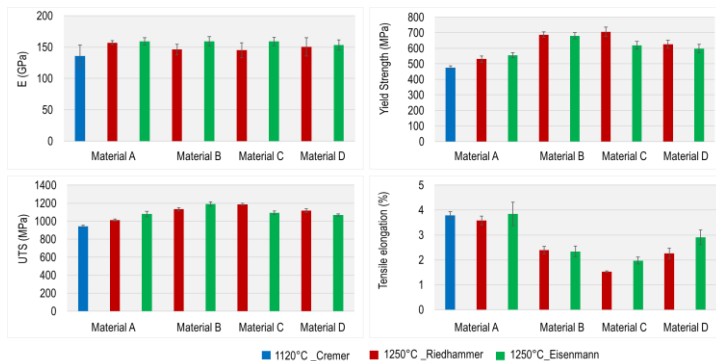


Figure 69 – Tensile properties of all materials tested on the second part of the project.

By analysing material A, it is possible to observe the influence of the sintering temperature on tensile properties. While there is a clear trend of increasing the Young's modulus, yield strength and ultimate tensile strength, there is almost no

4. Results and Discussions

change on the tensile elongation. The effect of the increase in the sintering temperature in this material is due to the combination of the effects of the increased fraction of the load bearing section and decreased amount of Ni-austenite. These two effects have a synergistic effect on stiffness and strength, and an opposite effect on ductility. Tensile elongation does not change with sintering temperature since the two effects offset each other. Strength and ductility are slightly higher in pieces sintered in Eisenmann furnace due to the higher densification.

The Young's modulus of materials B, C and D are slightly higher for the samples sintered in the Eisenmann furnace, again due to the higher densification. Tensile strength and ductility of material B is almost independent on the sintering cycle, coherently with the microstructure that, as discussed in the specific section, is not affected by the sintering cycle significantly. Materials C and D display a higher strength and a lower ductility when sintered in the Riedhammer furnace, still coherently with the microstructure that contains a higher percentage of martensite than when sintered in Eisenmann furnace. The three materials sintered at high temperature display different properties: higher strength for B and C, higher ductility for D. Even this observation finds a justification in the microstructure since material D contains the higher amount of bainite among the three materials.

The Charpy impact test results are presented in Figure 70. Material A presented an increase in impact strength with the sintering temperature, due to the enhanced strength and stable ductility. Impact strength of the three materials sintered at high temperature is coherent with ductility, as usual.

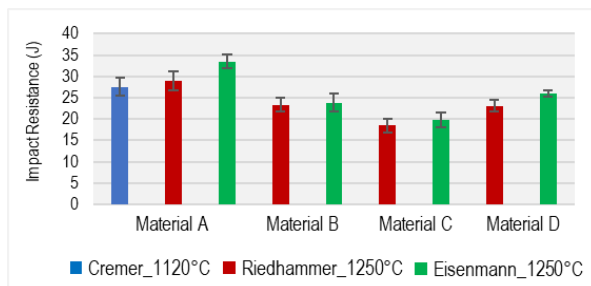


Figure 70 – Results of the measured impact resistance for all materials tested on the second part of the project.

4. Results and Discussions

The mechanical properties of the three materials sintered at high temperature are determined by their microstructure that, in turn, depends on the sintered carbon content. This last parameter may be adjusted to enhance either strength or ductility, to tailor the resulting properties to the specific application. The tensile properties of the reference material are significantly different from what it may be expected from sintering at standard temperature with the same density: 400 MPa Yield Strength, 740 MPa UTS, 2.6% Tensile Elongation [69]. The differences may be attributed to the higher cooling rate of the present work than that of the sintering cycle to which these data refer (0.8 °C/s).

With reference to the main scope of the present work it is interesting to compare the mechanical properties of the three steels sintered at high temperature with those of the reference steel sintered at 1120°C. This allows the verification of the possibility to compensate the absence of Ni (or the great reduction of its content) with the increment in the sintering temperature. For this purpose, the increment of the yield and tensile strength, the tensile elongation and the impact strength is shown in Figure 61.

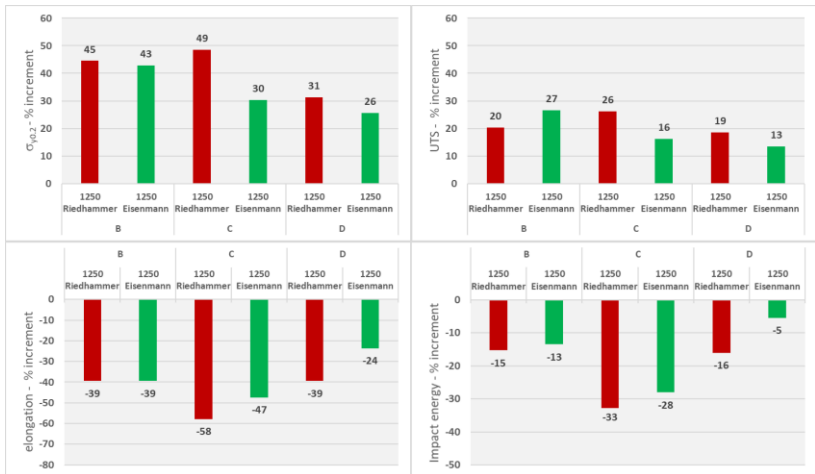


Figure 71 – increment of mechanical properties of HTS steels with respect to 1120°C sintered material A

The figure shows the very large increment in tensile strength achieved with the three steels, and the corresponding decrease of tensile elongation and impact strength. This comparison is mostly attributable to the absence (or very small amount) of Ni in the three steels that is not fully compensated by the improved pore morphology resulting from sintering at high temperature. The result is strongly dependent on the microstructure. As said above, the properties of the three steels may be tailored to specific applications by changing the carbon content. This will have an impact on the comparison with the reference material. For instance, a decrease of the carbon content might result in a lower strength compensated by a higher ductility and impact strength. This hypothesis needs for an experimental verification, and this could be a subject for a further work.

5. Conclusions

On the first part of this project, five different materials with different contents of nickel were used to investigate the effect of the sintering temperature on the dimensional precision, density, geometrical characteristics, pore morphology, and microstructure. Density slightly increases with sintering temperature.

Materials decrease their volume with sintering and the dimensional changes are increased with the sintering temperature. The dimensional precision of the specimens tends to decrease after sintering, and the results expressed in ISO IT tolerance classes were not affected by the sintering temperature.

The geometrical characteristics analysed were not affected by the sintering temperature and all the values obtained are aligned with the press and sintered typical results. The parallelism between the top and bottom surfaces, their flatness and the perpendicularity of the external cylindrical surface tend to be higher after sintering whereas cylindricity of the two cylindrical surfaces, their coaxiality and the perpendicularity of the internal cylindrical surface either reduces or remain the same. The dimensional precision and the geometrical stability of the rings investigated were not impaired by high temperature sintering (1250°C).

Density increases with the sintering temperature and hence porosity decreases. At the same time, pores become rounder and pore morphology is improved. The combination of all precedent factors leads to an increase in the fraction of the load bearing section.

Diffusion bonded steels present Ni austenite regions when sintered at 1120°C. These regions tend to decrease when the sintering temperature is raised, leading to an increased homogenization of the Ni distribution into the alloy. In fact, all microstructures tend to be more homogenous at higher sintering temperatures.

The combination of the microstructural analysis with pore morphology provides enough data to predict the influence of the sintering temperature in the mechanical properties. The tensile ductility is likely to increase with the sintering temperature for the Ni-free materials due to the higher fraction of the load bearing

section. This effect is partially counterbalanced in Ni-containing materials by the decrease in Ni austenite regions.

High temperature sintering should lead to higher tensile strength in all materials tested.

As per the complex design specimens investigated on the second part of the project, the results of dimensional changes confirmed what has been observed on the investigation of the ring-shaped specimens. The scatter of the dimensional change is the same as for those sintered at 1120°C and high temperature sintering does not impair the dimensional and geometrical precision of all 3 complex designs investigated.

HTS promotes a slightly higher density allied with improved pore morphology in material A. The tensile and impact specimens sintered in the Eisenmann furnace reach a slightly but consistent higher density that agrees with the slightly larger shrinkage measured on the three parts.

Materials B,C and D present a mixed microstructure of bainite/martensite while material A presents the typical heterogenous microstructure when sintered at 1120°C that becomes more homogenous as the sintering temperature is increased.

The diffusion bonded reference steel presented increased tensile and yield strength while not reducing tensile elongation when sintered at higher temperatures, this combination leads to slightly higher impact resistance. This effect is caused by the improved homogenization of the microstructure and the decrease of the Ni austenite content compensated by the improved pore morphology.

Materials C and D present tensile strength is slightly lower and tensile elongation and impact strength are higher in parts sintered in the Eisenmann furnace. This trend is coherent with the hardness and microhardness measurements. Differences in tensile and impact properties of HTS steels are due to the different hardness, not to the slight differences in density.

Each mechanical property presented different increments with reference to material A sintered at the conventional temperature of 1120°C. While the yield strength increased from 26% to 49%, the increments in ultimate tensile strength ranged from 13% and 27%. These results were due to the higher density, better pore morphology and higher hardness. On the other hand, tensile elongation reductions ranged from -

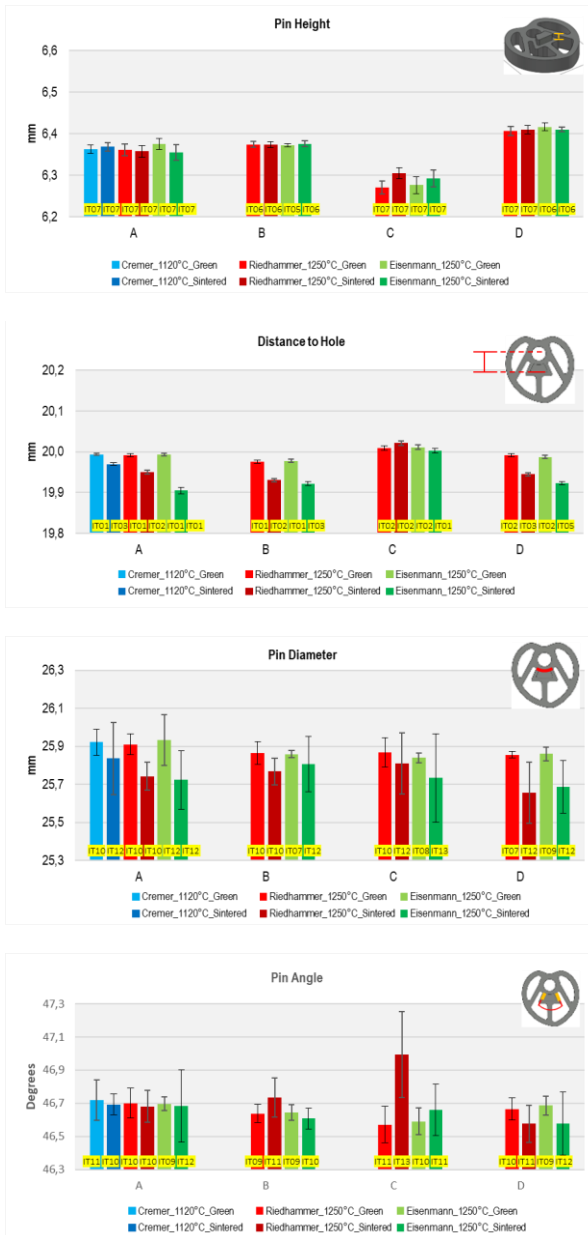
24% to -58% and the impact energy from -5% to -33%. The reductions in these mechanical properties happened due to the lack of Ni austenite regions attenuated by high density and better pore morphology. The material that presented the highest strength increment also showed the highest ductility and impact strength drop.

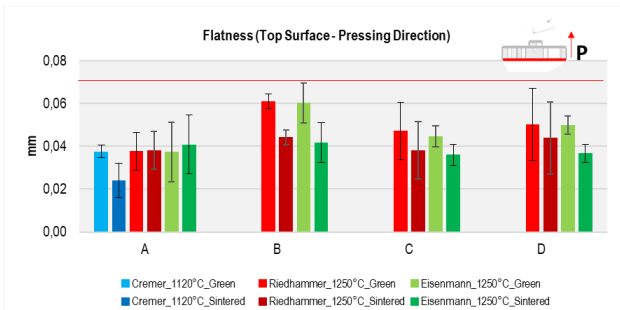
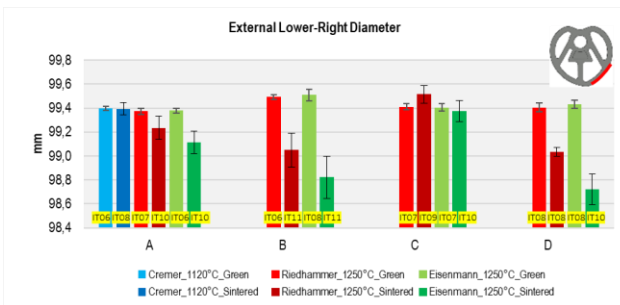
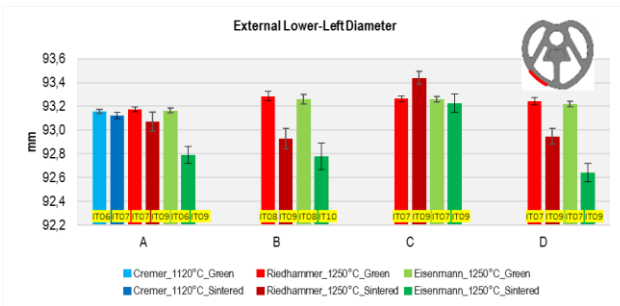
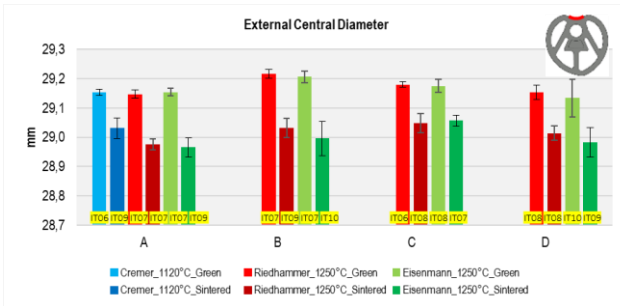
The different mechanical properties of materials B,C and D depend on their microstructure (bainite/martensite ratio) resulting from the different hardenability. These properties can be tailored via carbon content variation and cooling rate control after the sintering.

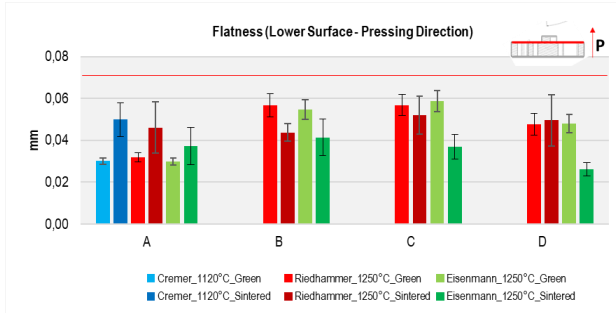
The higher hydrogen in the atmosphere may justify the smaller decarburization in the Eisenmann furnace, other than the slightly higher densification. This effect can be explained by the Cr-alloyed powders (materials B,C and D) reactions that happen during the sintering. At first, the reduction of the total oxygen of the material protecting carbon from oxidating at high temperature (deoxidation without decarburization). It is enhanced by the hydrogen partial pressure in the atmosphere and by a slow heating rate. Then, oxygen is stabilized in the chromium oxide since it cannot be reduced by hydrogen significantly. When the sintering temperature is achieved, less deoxidation and decarburization is observed.

HTS is a viable process to produce PM parts with similar dimensional tolerances as today produced usually at 1120-1150°C in belt furnaces. This project sets the blueprint for different alloys to be processed by high temperature sintering in a continuous furnace in the future.

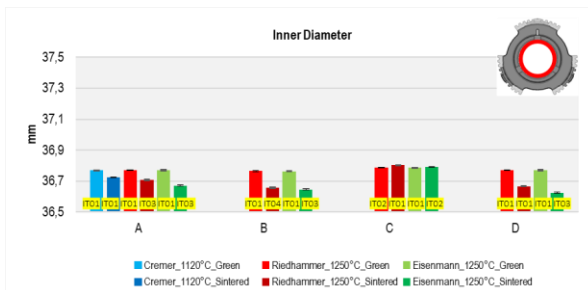
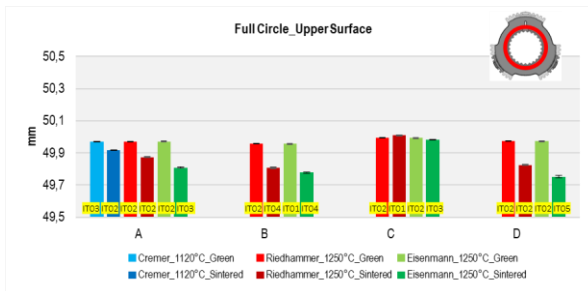
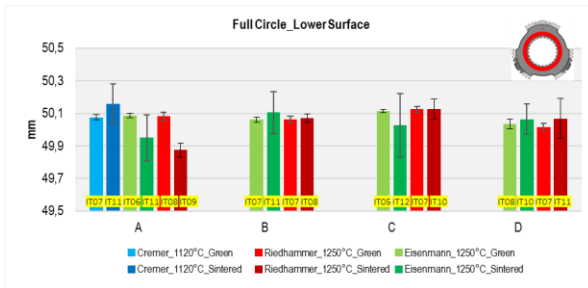
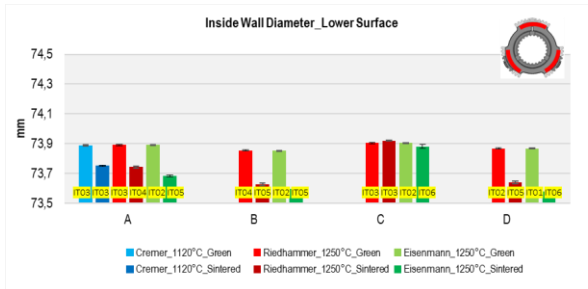
6. Appendix A

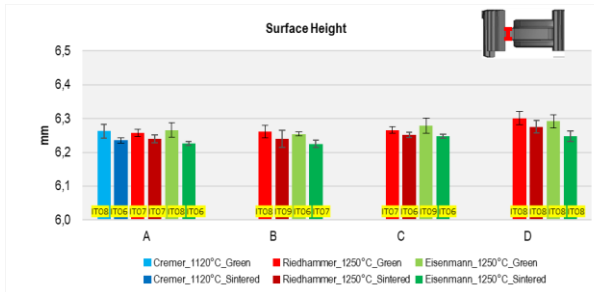
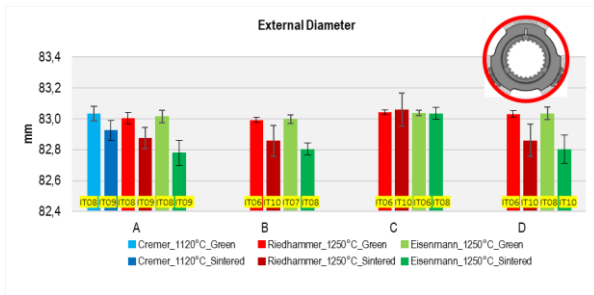
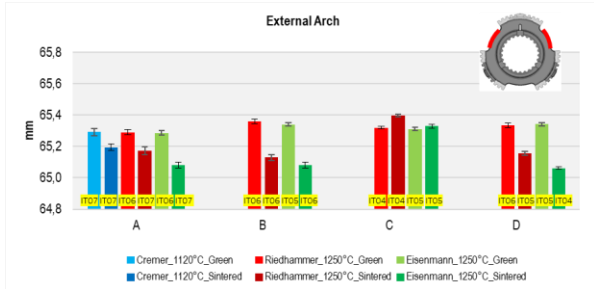


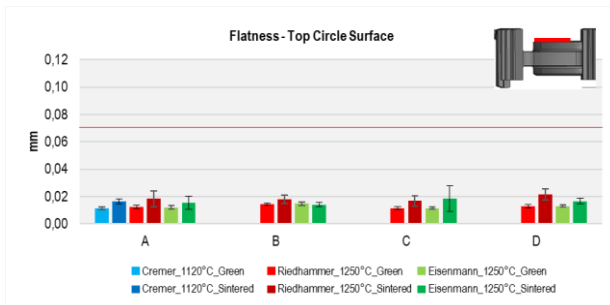
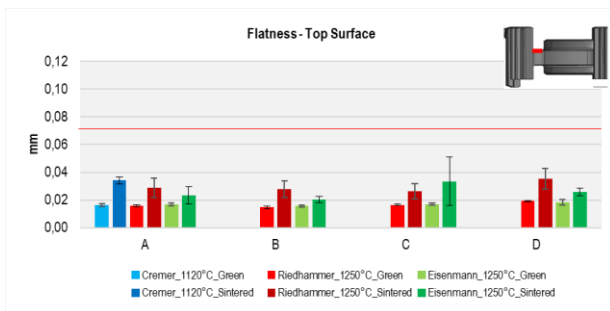
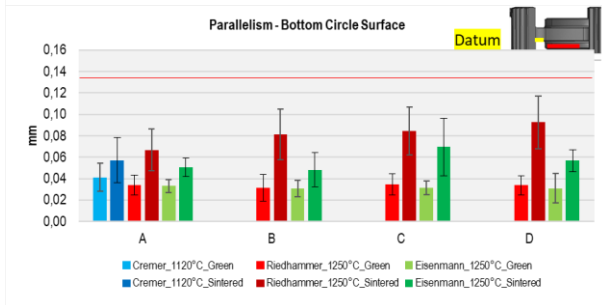
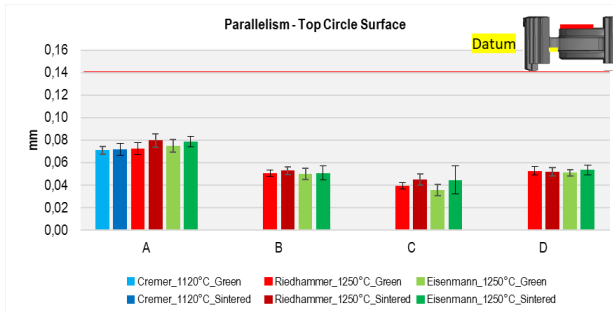


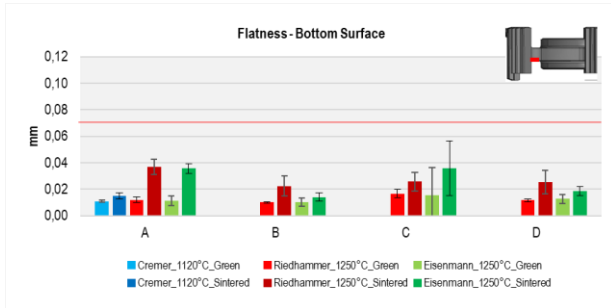


7. Appendix B

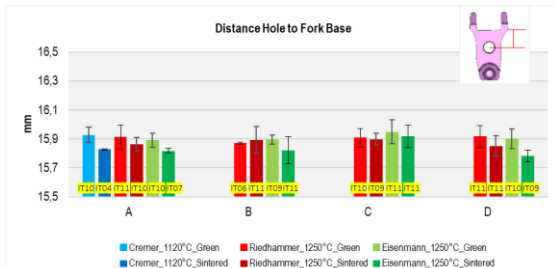
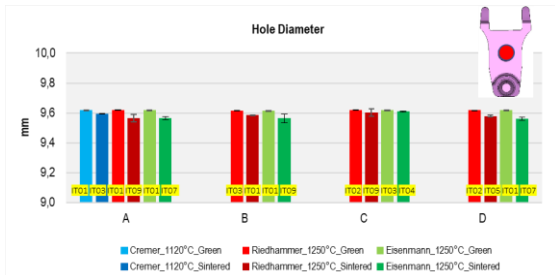
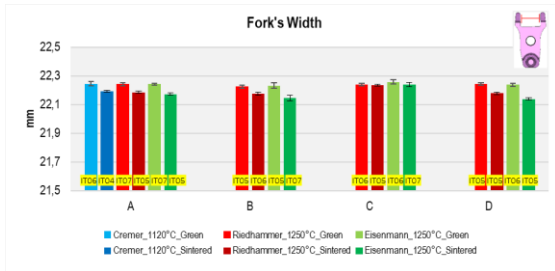
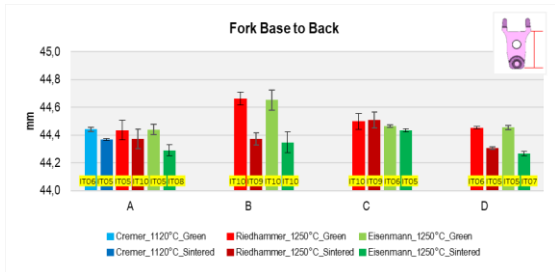


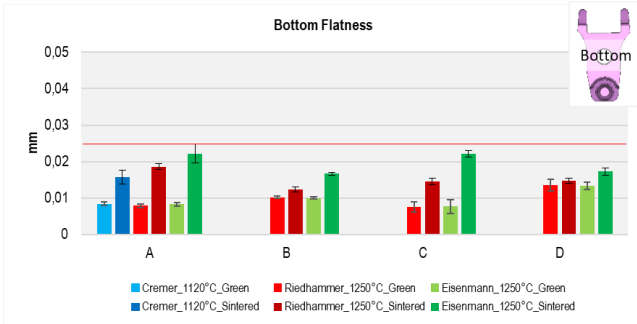
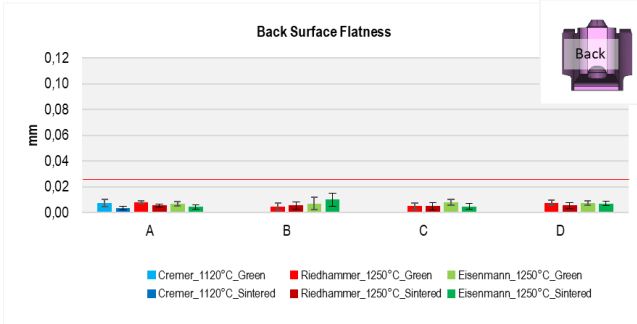






8. Appendix C





9. References

- [1] R. M. German. Powder metallurgy science. Metal powder industries federation (MPIF), 1984.
- [2] A. Sälak. Ferrous powder metallurgy. Cambridge International Science Publishing, 1995.
- [3] R. Morris. (2018). Electric vehicles revolution and implications for new energy metals. Online, Available from: <http://www.vale.com>.
- [4] London Metal Exchange, (2021), Online, Available from: <https://www.lme.com/metals>.
- [5] European Chemical Agency. (2018). Committee of risk assessment: opinion on scientific evaluation of occupational exposure limits for Nickel and its compounds (ECHA/RAC/ A77-O-000001412-86-189/F). Helsinki, FN: Registration, Evaluation, Authorization and Restriction of Chemical.
- [6] H. Danninger, R. de Oro Calderon, C. Gierl-Mayer. Chemical reactions during sintering of PM steel compacts as a function of the alloying route. Powder Metall. 2018;61(3):241–250.
- [7] U. Engstrom. High performance P/M materials by warm compaction of Densmix powders. Adv Powder Metall Part Mater. 1999;2(7):171–184.
- [8] A. Pietrovski, G. Biallas. Influence of sintering temperature on pore morphology, microstructure, and fatigue behaviour of MoNiCu alloyed sintered steel. Powder Metall. 1998;41(2):109–114.
- [9] G.F. Bocchini. Influence of process parameters on precision of PM parts. Powder Metall. 1985;28(3):155–165.
- [10] I. Cristofolini, A. Rao, C. Menapace, et al. Influence of sintering temperature on the shrinkage and geometrical characteristics of steel parts produced by powder metallurgy. J Mater Proc Techn. 2010;210:1716–1725.
- [11] I. Cristofolini, M. Pilla, A. Rao, et al. Dimensional and geometrical control of PM parts sintered at low and high temperatures. Adv Powder Metall Part Mater. 2010;1:19–26.

- [12] I. Cristofolini, A. Molinari, S. Tesfaye, et al. High temperature sintering: microstructure, density, dimensional and geometrical precision. *Adv Powder Metall Part Mater.* 2014;5:213–221.
- [13] I. Chang, Y. Zhao, *Advances in Powder Metallurgy: Properties, Processing and Applications.* Woodhead Publishing Series in Metals and Surface Engineering, Elsevier Science, 2013.
- [14] R. M. German, *Powder Metallurgy of Iron and Steel.* Eds. John Wiley & Sons, Inc. 1998
- [15] J. Secondi. Modelling powder compaction: from a pressure-density law to continuum mechanics. *Powder metallurgy*, 2002,45(3):213–217.
- [16] L. Parilak., E. Dudrova, R. Bidulsky, M. Kabatova, Derivation, testing and application of a practical compaction equation for cold die-compacted metal powders. *Powder Technology*, 2017,322:447–460
- [17] G. Aryanpour, M. Farzaneh. Application of a piston equation to describe die compaction of powders. *Powder Technology*, 2015;277:120–125.
- [18] A. Molinari, I. Cristofolini, G. Pederzini, and A. Rambelli. The densification equation in uniaxial cold compaction of a water-atomized 316L stainless steel powder. *International Journal of Powder Metallurgy*, 2017;53(3):41–48.
- [19] A. Molinari, I. Cristofolini, G. Pederzini, and A. Rambelli. A densification equation derived from the stress-deformation analysis of uniaxial cold compaction of metal powder mixes. *Powder Metallurgy*, 2018;61(3):210–218.
- [20] I. Cristofolini, A. Molinari, M. Zago, G. Pederzini, and A. Rambelli. The analysis of the densification curve of metallic powders in uniaxial cold compaction. *Advances in Powder Metallurgy and Particulate Materials. Proceedings of the 2019 International Conference on Powder Metallurgy and Particulate Materials*, 2020:30–41.
- [21] D. Miligan, U. Engstrom, S. Smith. High Temperature Sintering – A Cost Effective Way to Future High-Performance Materials. *Proceedings PM²TEC 2005*, Canada. 2005;1:1-5
- [22] A. Tims, R. Warzel III, B. Hu. *Manufacturing Methods for High Density Powered Metal (PM) Applications and Their Mechanical Properties.* 531-535

- [23] A. Pietrowski, G. Biallas. Influence of sintering temperature on pore morphology, microstructure, and fatigue behaviour of MoNiCu alloyed sintered steel. *Powder Metall.* 1998;41(2):109-114
- [24] Höganäs AB. Höganäs Handbook for Sintered Components – Design and Mechanical Properties, 2004 Höganäs AB, Höganäs Sweden.
- [25] M. Puszcz, M. Signorini, A. Molinari, G. Straffelini. Image analysis investigation of the effect of the process variables on the porosity of sintered chromium steels. *Mater. Char.* 2003;50(1):1-10
- [26] P. Beiss, Dalgic M. Effect of pore structure on bending fatigue strength of sintered steel. *Adv Powder Metall Part Mat* 1996;13:140-153
- [27] P. Beiss, S. Lindlohr. Porosity statistics and fatigue strength. *International Journal of Powder Metallurgy* 2009;45:39-48
- [28] Y. Murakami. *Metal Fatigue: Effects of Small Defects and Non-metallic Inclusions*; Elsevier, Amsterdam, 2002
- [29] D. Toledo Dos Santos, A. Salemi, I. Cristofolini, A. Molinari. The tensile properties of a Powder Metallurgy Cu–Mo–Ni diffusion bonded steel sintered at different temperatures. *Materials Science & Engineering.* 2019;759:715-724
- [30] V. Stoyanova, A. Molinari. Vacuum Sintering and Sinter-Hardening of Mo and Ni low alloyed steels. *Powder Metallurgy Progress.* 2004;4(2):79-87
- [31] P. Shen, R. Shivanath. Effect of sintering temperature on the as-sintered and heat treated properties of pre-alloyed Mo low carbon steel alloyed with ferromanganese. *Proceedings AMPM2019. USA.* 2019;:611-624
- [32] B. Lindsley. Mn-containing Steels for High-Performance PM applications. *Powder Metallurgy Industry.* 2011;(6):1-7
- [33] E. Hryha, E. Dudrova, L. Nyborg. Critical Aspects of Alloying of Sintered Steels with Manganese. *Metallurgical and Materials Transactions.* 2010;41(11):2880-2897
- [34] N. Kariyawasam, D. Malakhov, R. Lawcock. A computational experimental approach to understanding the homogenization behaviour of alloying elements during the sintering of PM Steel. *Advances in Powder Metallurgy & Particulate Materials.* 2017:56-60
- [35] R.M. German. *Powder Metallurgy Science.* 1994: Metal Powder Industries Federation.

- [36] L. Wimbert, M. Kylan McQuaig, B. Lindsley. Mechanical Properties of a New Class of High Temperature Sintering Alloys. Proceedings EUROPM2019. Netherlands. 2019
- [37] C. Shade, T. Murphy, A. Lawley, R. Doherty. Microstructure and mechanical properties of PM steels alloyed with silicon and vanadium. International Journal of Powder Metallurgy . 2012;48(6):41-48
- [38] B. Lindsley, C. Shade, T. Murp. Vanadium and silicon alloyed PM steels. Proceedings EUROPM2013 Congress & Exhibition. Sweden. 2013;3:307-312
- [39] K. McQuaig, A. Wartenberg, B. Lindsley, T. Murphy. Advanced Material Options for High Temperature Sintering. 2019;:625-638
- [40] R. Oro, M. Jalilizyaeian, J. Dunkley, C. Gierl-Mayer, H. Danninger. The Real Benefits of High Sintering Temperatures on the Properties of Low Alloy Sintered, Proceedings EuroPM2018 Congress & Exhibition. Spain
- [41] M. Sundaram, S. Karamchedu, C. Gouhier, E. Hryha, O. Bergman, L. Nyborg. Vacuum Sintering of Chromium Alloyed Powder Metallurgy Steels. Metal Powder Report.2019;74(5):244-250
- [42] V. Stoyanova, G. Straffelini, A. Molinari. Influence of Microstructure and Microhardness on Impact Properties of High Density Cr and Mo Low Alloyed Sintered Steels. Powder Metallurgy Progress.2004;4(4):243-255
- [43] V. Stoyanova, A. Molinari. As Sintered Tensile and Impact Properties of High Density Fe-1,5Cr-0,2Mo Sintered Steel. Powder Metallurgy Progress.2003;3(2):86-93
- [44] S. Baselli, A. Molinari, Sintering shrinkage of uniaxial cold compacted iron: a new shrinkage kinetic equation accounting for the microstructure of green parts. Powder Metallurgy.2019;62(1):1-7.
- [45] M. Zago, M. Larsson, I. Cristofolini. An improved design method for net-shape manufacturing in powder metallurgy. Lecture Notes in Mechanical Engineering. Springer Nature Switzerland.2020;:257-267
- [46] I. Cristofolini, A. Molinari, M. Zago, S. Amirabdollahian, O. Coube, M. J. Dougan, M. Larsson, M. Schneider, P. Valler, J. Voglhuber, L. Wimbert, Design for sintering club project – dealing with the anisotropy of dimensional changes in real parts, EuroPM2018 Congress & Exhibition, Bilbao (Spain).

- [47] I. Cristofolini, A. Rao, C. Menapace, A. Molinari. Influence of Sintering Temperature on the Shrinkage and Geometrical Characteristics of Steel Parts Produced by Powder Metallurgy. *Journal of Materials Processing Technology*.2010;210:1716 - 1725
- [48] I. Cristofolini, A. Molinari, S. Tesfaye, M. Federici, H. Weber, A. Nicolò. High Temperature Sintering: Microstructure, Density, Dimensional and Geometrical Precision. *Proceedings WorldPM2014. International Conference 18-22 May 2014. USA. Ed. EPMA.*
- [49] F. D. Richardson, J. H. E. Jeffes. The Thermodynamics of Substances of Interest in Iron and Steel Making from 0°C to 2400°C I-Oxides. *Journal of the Iron and Steel Institute*.1949;160:261-270
- [50] J. O. Andersson, T. Helander, L. Höglund, P. F. Shi, B. Sundman. Thermo-Calc & DICTRA, computational tools for material science. *Calphad*.2002; 26:273-312.
- [51] O. Bergman. Influence of Oxygen Partial Pressure in Sintering Atmosphere on Properties of Cr-Mo Prealloyed Powder Metallurgy Steel. *Powder Metallurgy*. 2007;5(3):243-249
- [52] O. Bergman, L. Nyborg. Evaluation of Sintered Properties of PM Steels based on Cr and Cr-Mn Prealloyed Steel Powders. *Powder Metallurgy Progress*. 2010;10:1-19
- [53] H. Danninger, C. Gierl, S. Kremel, G. Leitner, K. Jaenicke-Roessler, Y. Yu. Degassing and Deoxidation Processes During Sintering of Unalloyed and Alloyed PM Steels *Powder Metallurgy Progress*. 2002;2:125-140
- [54] S. Kremel, H. Danninger, Y. Yu. Effect of sintering conditions on particle contacts and mechanical properties of PM steels prepared from 3%Cr prealloyed powder. *Powder Metallurgy Progress*. 2002;2:211-221
- [55] E. Hryha, L. Cajkova, E. Dudrova, L. Nyborg. Study of Reduction/Oxidation Processes in Cr-Mo Prealloyed Steels during Sintering by Continuous Atmosphere Monitoring. *Proceedings of EUROPM2008, Germany*. 2008;1:108-114
- [56] M. Jaliliziyaean, C. Gierl, H. Danninger. Effect of prealloyed Mn and Cr on chemical reactions during sintering of steel compacts. *Advances in Powder Metallurgy & Particulate Materials*. 2008;5:72-78

- [57] C. X. Liu, L. Nyborg, T. Tunberg. Enhanced vacuum sintering of water-atomized austenitic stainless steel powder by carbon addition increases product properties. *Adv. Powder Metall. Part. Mater.* 1992;3:383–396
- [58] W. Gruner, S. Stolle, K. Wetzig. Formation of CO x species during the carbothermal reduction of oxides of Zr, Si, Ti, Cr, W, and Mo. *International Journal of Refractory Metals & Hard Materials.*2000;18:187-145
- [59] L. M. Berger, S; Stolle, W. Gruner, K. Wetzig. Investigation of the carbothermal reduction process of chromium oxide by micro-and lab-scale methods. *International Journal of Refractory Metals & Hard Materials.* 2001;19(2):109-121
- [60] H. Danninger, C. Xu. De-gassing and reduction during sintering of high density PM steels. *Proceedings of EUROPM2003, Spain. EPMA.* 2003;1:269-274
- [61] ISO 10360-5:2020. Coordinate measuring machines (CMMs) using single and multiple stylus contacting probing systems using discrete point and/or scanning measuring mode; 3. Available from: <https://www.iso.org/standard/73431.html>
- [62] S. Sainz, W. Garcia, A. Karuppanagounder. Microstructural development during sintering of PM steels with admixed nickel. *Powder Metall Prog.* 2017;7:121–127
- [63] 'Guida alla progettazione dei componenti sinterizzati', Available from: www.metallurgia-italiana.net
- [64] F. Castro, A. Veiga, S. Sainz, A. Karuppanagounder, D. Jorge. Influence of sintering cycle and chemical composition on the amount of martensite obtained after cooling of PM nickel steels. *Proceedings EuroPM2013, Gothenburg (Sweden)* 15-18 September (2013)
- [65] G. Straffelini, C. Menapace, A. Molinari. Interpretation of effect of matrix hardness on tensile and impact strength of sintered steels. *Powder Metall.* 2002;45 (2):167–176
- [66] M.F. Ashby, L.J. Gibson. *Cellular Solids.* Pergamon Press;1988
- [67] Y. L. Cope, *Metallurgia.*1965;72:165.
- [68] D. Toledo Dos Santos, A. Salemi, I. Cristofolini, A. Molinari. The tensile properties of a Powder Metallurgy Cu–Mo–Ni diffusion bonded steel sintered at different temperatures. *Materials Science & Engineering.* 2019;A 759:715-724
- [69] Höganäs Handbook: Iron and Steel Powders for Sintered Components 2017.

10. Scientific production

Articles published in international journals:

D. Toledo Dos Santos, A. Salemi, I. Cristofolini, A. Molinari. *The tensile properties of a Powder Metallurgy Cu–Mo–Ni diffusion bonded steel sintered at different temperatures*. Materials Science & Engineering. 2019;A 759:715-724

D. Toledo dos Santos, M. Zadra, L. Girardini, P. Albonetti, S. Bordin, A. Molinari. *Influence of die wall lubrication on tensile properties of high temperature sintered and sinterhardened low alloy steel*. Powder Metallurgy. 2020;63(4):268-276

D. Toledo, I. Cristofolini, A. Molinari, V. Arnhold, V. Kruzhanov, P. Vervoort, M. Dougan, L. Wimbert, V. Bonnefoy, R. Hellein, H. Weber, F. Baumgärtner, J. Sicre, C. Larsson, M. Schneider. *High temperature sintering and its effect on dimensional and geometrical precision and on microstructure of low alloyed steels*. Powder Metallurgy . 2020;63(2):80-93

Article published in congress/proceedings:

D. Toledo, I. Cristofolini, A. Molinari, V. Arnhold, V. Kruzhanov, P. Vervoort, M. Dougan, L. Wimbert, V. Bonnefoy, R. Hellein, H. Weber, F. Baumgärtner, M. Fernandez, C. Larsson, M. Schneider. *High temperature sintering of low alloy steels: effect on shrinkage and dimensional stability*. Proceedings EUROPM2019 Congress and Exhibition, Maastricht (The Netherlands), 13-16 October 2019, ed. EPMA, Shrewsbury (UK), ed. EPMA, Shrewsbury (UK), CD room, ISBN:978-1-899072-51-4

11. Acknowledgements

I would like to express my gratitude to everyone who was part of this project, specially to Professor Alberto Molinari for the opportunity and the trust imbedded to me. The knowledge and the friendship we built in the last years will be forever remembered. I would like to thank Professor Ilaria Cristofolini for the expertise she devoted to each analysis of the countless investigations we performed using the CMM machine, it was for sure a long road we covered together and the highlight of the content in this thesis.

I would like to thank my peers in the doctorate school of the 32nd cycle, Marco Zago, Ana Paula, Murilo, Baland, Sunil, Pryia, Michele, Giulia, Samuel, Matteo, Sasan and Faraz. The partnership we did to perform great research in our fields was amazing and very fruitful to me. Friendship is the foundation to happiness and I feel lucky to be able to share it with you.

Regarding the opportunity to be part of the EPMA club project, I would like to thank all companies that were part of this: Hoeganaes AB, GKN Höganäs, GKN Sinter Metals, Miba, Riedharmmer, Schunk, Ames, Eisenmann, Pometon SpA, PM Consulting, PM Solutions and the University of Trento. They provided the materials and equipments to make this thesis possible. Their faith and funding in materials engineering is what push science forward and help society to thrive.

Thank you to my parents, João and Fernanda, and my brother José. You are my role models and why I believe that education is a tool to transform lives. And finally, thank you to my wife Mariana and my little ones, Sophia and Olivia, for believing in my dreams and pushing me forward always.